Timing Noise Characterization of High-Speed Digital Bit Sequences Using Incoherent Subsampling and Algorithmic Clock Recovery

Hyun Woo Choi, *Member, IEEE*, Thomas Moon, *Student Member, IEEE*, and Abhijit Chatterjee, *Fellow, IEEE*

***Abstract*— In this paper, we exploit a software-based nonreal-time signal acquisition technique to enable high-precision jitter characterization of multi-Gb/s pseudorandom bit sequences (PRBSs) with minimal hardware support. For signal acquisition, incoherent subsampling is employed to increase the effective sampling rate of a digitizer and to simplify its signal acquisition architecture by removing the need for timing synchronization circuits. As a substitute for hardware synchronization circuits, the multiple stages of discrete frequency estimation algorithm, called algorithmic clock recovery (CR), are used. Using the frequency estimate obtained from the proposed algorithmic CR allows us to digitally reconstruct an incoherently subsampled PRBS into a single period of the signal in the discrete-time-domain. The proposed algorithmic CR is accurate and robust, especially in the presence of signal noise and multiple aliased distortions as compared with previously published approaches. In addition, the proposed all-digital jitter characterization technique (including self-reference signal extraction) enables data-dependent jitter separation without using the tail-fitting of a jitter histogram.**

***Index Terms*— Noise measurement, sampling methods, signal reconstruction, signal sampling, time measurement, timing jitter.**

I. Introduction

NONREAL-TIME jitter analyzers are considered practical, low-cost test instruments since they do not require samplers whose sampling speed is multiple times faster than the signal being tested. Even though some cutting-edge real-time oscilloscopes are already equipped with over 60-Gsps real-time sampling capability, the use of nonreal-time (or subsampling) measurement techniques is still valuable in the sense that nonreal-time jitter analyzers (or oscilloscopes) are able to acquire high-speed test signals with a much slower sampling speed, which can help reduce the cost of tests and measurements. In wireless/RF testing, the direct subsampling of an RF carrier signal without using a frequency mixer is used for a wideband multistandard data acquisition and receiver testing [1], [2].

Manuscript received September 29, 2013; revised February 23, 2014; accepted February 24, 2014. Date of publication May 7, 2014; date of current version November 6, 2014. This work was supported by the National Science Foundation under Grant CCR-0834484. The Associate Editor coordinating the review process was Dr. John Lataire.

The authors are with the Georgia Institute of Technology, Atlanta, GA 30332 USA (e-mail: hyun@gatech.edu).

Digital Object Identifier 10.1109/TIM.2014.2322713

In comparison, for digital serial data testing, nonreal-time jitter analyzers employ coherent subsampling instruments, which are further divided into random and sequential equivalent-time sampling schemes. These two types of nonreal-time sampling are commonly used to acquire high-speed signals for jitter testing because they acquire point samples over many repetitions of the input periodic signal to increase the effective sampling rate of digitizers. However, the effective sampling rate can be increased only if the coherent subsampling method is provided additional RF/mixed-signal circuitry to reconstruct the original waveform from the subsampled signal. For instance, the random equivalent-time sampling requires a time-to-digital converter (TDC) and an explicit trigger signal, and the sequential equivalent-time sampling needs a sequential delay generator. These additional timing subsystems incorporated into coherent subsampling instrument complicate the overall architecture of nonreal-time jitter analyzers and their experiment setups. In addition, the measurement uncertainty induced by nonidealities of the additional timing subsystems may limit the overall performance of jitter measurement.

These technical difficulties may be overcome with the development of various software-synchronization techniques, which can be used in an incoherent subsampling environment [3]–[14]. Commercial vendors such as Tektronix or Lecroy developed a software-synchronization technique, called software phase-locked loop (PLL) as a software package for their cutting-edge oscilloscopes, which is used both to compensate for low-frequency change of reference edge timing and to perform software-based synchronization [3], [4]. This technique is enabled using jitter tracking digital filters whose characteristics are determined based on the required jitter compensation bandwidth (further details, however, have not been published). However, this software PLL requires oversampling of the signal being tested, which can be done only with cutting-edge oscilloscopes. Such high-speed oversampling is an expensive solution and not readily available in many kinds of test equipment. In optical sampling research, various software-synchronization techniques have been used. In [5]–[7], the periodogram of the incoherently sampled signal was used to estimate the discrete frequency (or period) value of the sampled signal. Such a standard

Fourier transform-based spectral analysis may be used only for online bit error rate monitoring that does not require very accurate synchronization, but it may not be used for the precision measurement that needs to be performed in the presence of noise, jitter, and multiple aliased harmonic tones. In comparison, we use a type of periodogram (with spectral interpolation) as the first stage of the proposed software synchronization algorithm, called the coarse discrete frequency estimation. In [8], the binary-tree data-truncation algorithm was used to reduce the computation time required to evaluate the periodogram of the sampled signal. This technique helps reduce computation burden and is beneficial for real-time synchronization. Due to its inherent frequency resolution limitation, this approach alone, however, may not be used for precision measurement.

To enhance synchronization accuracy, [9], [10], [15] introduced a chirp z-transform (CZT)-based software synchronization technique. The synchronization accuracy obtainable from this enhanced spectral analysis approach was found to be good enough for signal characterization purpose unless the fundamental tone of a sampled signal contained high-frequency jitter or the aliased harmonics and distortions (due to subsampling) were placed very near the fundamental tone, which compromised the frequency estimation accuracy. In this paper, we evaluated the synchronization performance of the CZT-based technique and provided the comparison with our proposed algorithm (spectral jitter cost function described later) in Section III-A, especially in cases where the sampled signal was jittered and contained aliased distortions near the fundamental tone. In [11] and [12], another fine synchronization approach is proposed. This uses the statistical jitter quantity of the reconstructed eye-diagram as a cost function (we refer to this as a time-domain jitter cost function in this paper). However, the time-domain jitter cost function requires a large sample size, especially on the rising/falling edges of the signal, to generate a statistical jitter quantity. In addition, the technique does not provide a smooth cost function over the required frequency sweep range unless it is used for a very large number of samples. As an alternative to this time-domain jitter cost function, we use a spectral jitter cost function, which provides a smooth, reliable cost function as compared with the time-domain jitter cost function. The computation power required to generate the spectral jitter cost function is relatively low after using our selective harmonic nonequispaced spectral analysis approach, which is another contribution of this paper as compared with our prior publications. The performance comparison between the two approaches is provided in Section III-A.

In this paper, we exploit a software-based nonreal-time signal acquisition technique to enable high-precision jitter characterization of high-speed pseudorandom bit sequences (PRBSs) with simpler hardware configurations. First, the proposed method employs subsampling to increase the effective sampling rate of analog-to-digital (A/D) converters. Like other nonreal-time sampling methods, this approach avoids the shortcoming of real-time sampling oscilloscopes in generating an adequate sampling frequency to capture the highest data rates that exist today. Second, our method uses incoherent sampling to avoid the need for the complex timing circuitry that a coherent sampling device requires to synchronize the sampling rate. Third, we employ algorithmic clock recovery (CR) instead of using hardware CR subsystems. The proposed algorithmic CR approach differs from other algorithmic CR or software-synchronization techniques [5]–[12] in the following ways.

1) The accuracy of the proposed algorithmic CR (or software-synchronization) is enhanced using the spectral interpolation (coarse estimation in Section II-C1) and the selective discrete Fourier transform (DFT) frames (fine estimation in Section II-C2). The synchronization accuracy of the technique (without using the fine-tuning) is comparable with (or similar to) the chirp-z-based technique shown in [9] and [10], but we reduce the computational burden by sequentially narrowing the frequency range (or bandwidth) of spectral evaluation through multiple analysis steps.
2) In the fine tuning process, a spectral jitter cost function (Section II-C4) is used to enhance the frequency estimation accuracy and computational reliability, especially when the sampled signal contains jitter, aliased harmonics, and distortions near the fundamental tone. The spectral jitter cost function uses sparsity promotion in the frequency-domain, which is more stable than the time-domain cost function (shown in [11] and [12]), especially when the sample size is small. In addition, it performs significantly better when the signal being sampled contains inherent jitter as compared with the performance of the CZT-based synchronization.

The performance comparison between the proposed CR algorithm and other software synchronization techniques is provided in Section III-A. The proposed algorithmic CR method along with the self-reference extraction and jitter quantification algorithms, to be described later in this paper, alleviate the need for the hardware that is necessary with their hardware-based CR counterparts.

We previously published the core idea and proof-of-concept simulation results of this paper in [16]–[18]. In comparison with our previous work, this paper provides follow-up research findings, especially on the enhancement of the algorithmic CR accuracy using the DFT-frame-based spectral analysis and on the optimization of the computational efficiency of the proposed sparsity promotion algorithms. This optimization is made possible using the evaluation of spectral jitter cost functions for selective frequency bins, as shown in Section II-C4. In addition, this paper provides theoretical frameworks, a comparison of the proposed method with other software synchronization techniques, and supporting hardware measurement results.

II. Proposed Jitter Characterization Technique

A. Overview

The proposed jitter characterization technique simplifies the signal acquisition hardware of conventional sampling-based jitter characterization systems, which exploits their subsystems, in other words, the hardware CR circuit, TDC,

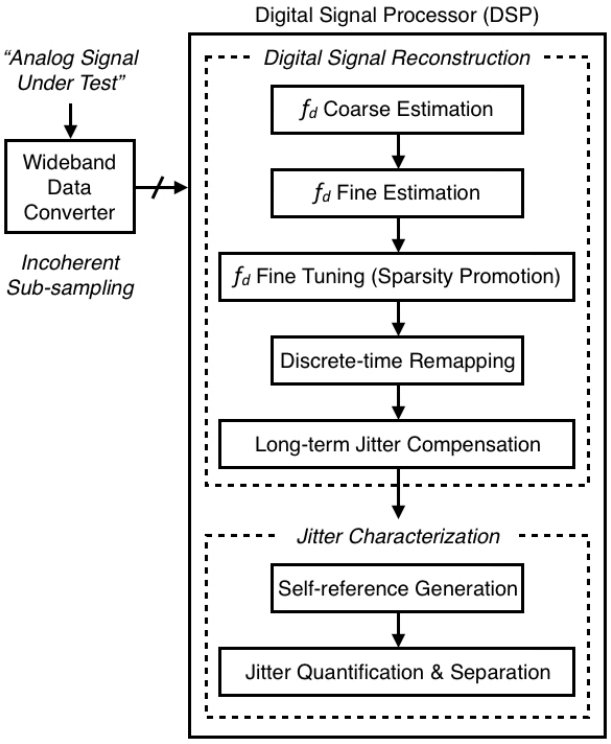

Fig. 1. Block diagram of the proposed jitter characterization method.

trigger signal generator, and delay generator. In comparison, the proposed system requires only a subsampling A/D converter, sampling oscillator, and DSP. In the proposed technique, the signal being tested is incoherently subsampled and reconstructed even when the signal frequency is not known. This sampling method alleviates the need for synchronizing the sampling clock frequency with the test signal frequency. The only requirement is that the input analog bandwidth of the sampler be wide enough to incorporate the potentially wide spectrum of the test signal.

In the proposed method, a PRBS test signal is incoherently subsampled even when the signal frequency is now known. A single period of the PRBS is digitally reconstructed from the obtained raw sample data using the algorithmic CR as described in Section II-C (a flowchart of the algorithms is shown in Fig. 1). The algorithmic CR is comprised of four steps: discrete fundamental frequency (f_d) coarse estimation, f_d fine estimation, f_d fine tuning, and discrete-time remapping. f_d coarse estimation (Section II-C1) uses a windowed DFT with digital pre and postconditioning techniques to coarsely estimate the discrete fundamental frequency of the sampled test signal by locating a spectral peak in the DFT spectrum. f_d fine estimation (Section II-C2) uses selective DFT frames to obtain an enhanced F_d value estimate. Discrete-time remapping ((Section II-C3) then uses the estimated f_d value when the raw sample indices of the test signal are remapped to time values in the discrete-time-domain, representing a single period of the test signal. In this way, the test signal is reconstructed. Optionally, a more enhanced f_d estimate can be obtained from the f_d fine tuning (Section II-C4), which uses spectral sparsity constrained optimization.

Jitter characteristics of the digitized PRBS can be quantified by analyzing the discrete-time values of the reconstructed PRBS samples as compared with a digitally generated self-reference signal, which is a virtual signal that is extracted from the reconstructed PRBS itself by applying wavelet-based denoising to the signal. The use of the self-reference signal removes the need for externally provided analog reference signals. Details of the self-reference signal extraction and jitter quantification procedures are provided in Sections II-D and E.

B. Incoherent Subsampling

A digitizer using a programmable oscillator as a sampling time-based is employed to incoherently subsample a continuous-time periodic test signal whose frequency is unknown and time-varying due to test signal instability. The time-base signal does not need to be synchronized in time or frequency with the test signal. Thus, no common time-based signal is required between the digitizer and the device under test, which generates the test signal. However, the analog input bandwidth of the digitizer should be wider than the test signal bandwidth to accommodate all the test signal frequency components, even when the sampling rate of the digitizer can be much lower than the Nyquist rate.

Suppose a continuous-time test signal that is periodic and normalized to zero-mean is given by

$$x(t) = x(t - T_x(t)) + n(t) \tag{1}$$

where $T_x(t)$ denotes the unknown and time-varying period value of the whole PRBS test signal, and $n(t)$ denotes amplitude noise, and the discrete samples of the test signal at n equally spaced coordinate points is obtained by

$$x[k] = x(k \cdot T_s) \quad \text{for } k = 1, 2, 3, \ldots, n \tag{2}$$

where T_s is the sampling interval and n is a power of 2. We can use a vector to denote the original samples: $\mathbf{x} = [x[1]\, x[2]\, x[3]\, \ldots\, x[n]]^\top$.

In cases where the test signal $x(t)$ is a PRBS, for the simplicity of notations, we redefine the Nyquist sampling rate as

$$f_N = \frac{2}{T_b} \tag{3}$$

where T_b denotes the bit width of the test signal, even though the test signal may contain frequency components beyond a frequency of $1/T_b$. The subsampling ratio R_s is accordingly defined by

$$R_s = \frac{f_N}{f_s} \tag{4}$$

where $f_s = 1/T_s$ denotes the sampling rate. In this paper, we consider the cases of incoherent subsampling, where R_s is larger than 1. Such an incoherently subsampled discrete signal in its raw format without signal reconstruction cannot be directly used for jitter analysis due to the effect of signal aliasing.

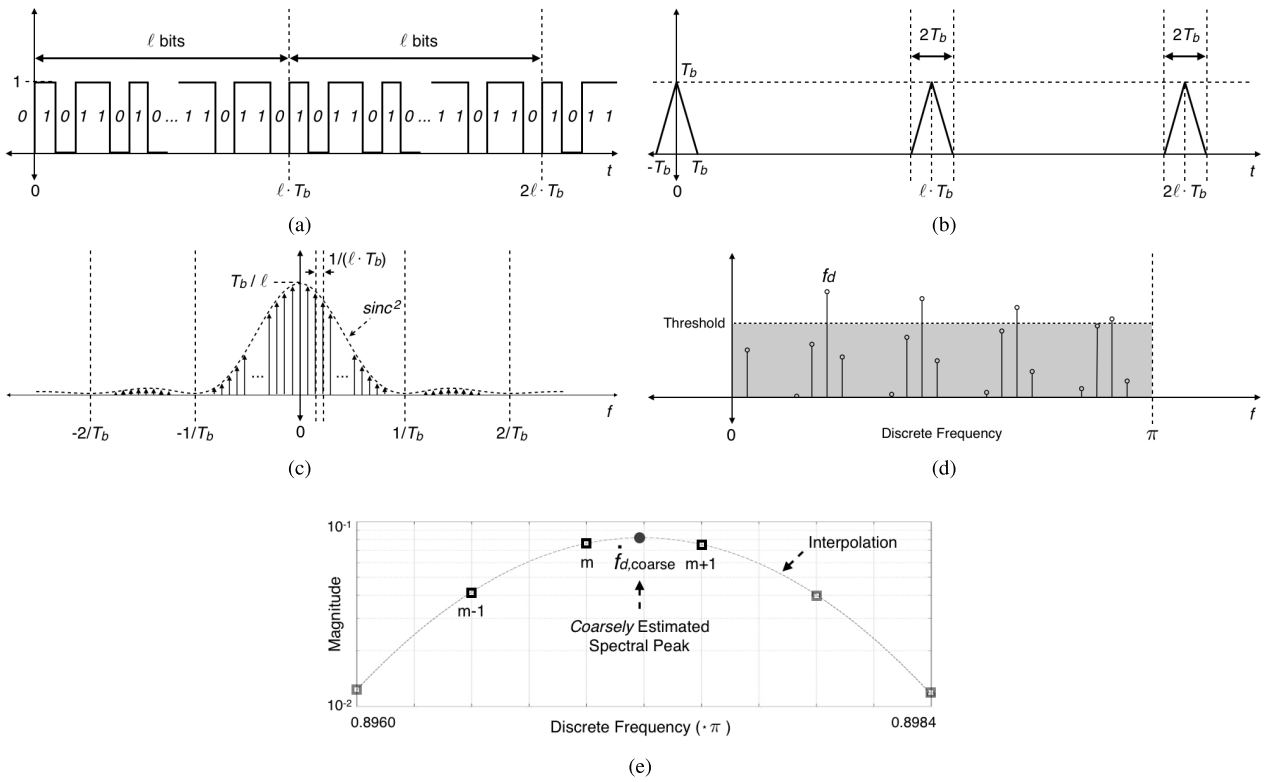

Fig. 2. Derivation of the power spectrum of a PRBS. (a) l-bit PRBS shown in the time-domain (T_b is the bit width). (b) Autocorrelation of the PRBS shown in (a). (c) Power spectrum of the continuous-time PRBS shown in (a). (d) Discrete power spectrum of the incoherently subsampled PRBS (an illustration, not from computer simulation). (e) Three-point estimation: the three spectral components (denoted by squares) near the discrete spectral peak of the fundamental tone (denoted by m) of the discrete power spectrum of the incoherently subsampled PRBS.

C. Digital Signal Reconstruction (Algorithmic CR)

In this section, we introduce a new algorithmic CR technique, which enables the reconstruction of an incoherently subsampled PRBS into a single period of the waveform in the discrete-time-domain. When the pattern length of the test PRBS is l, the PRBS pattern repeats every l bit, resulting in a periodic signal as shown in Fig. 2(a). Due to the periodicity, the discrete fundamental frequency (f_d) of the sampled PRBS can be identified from its frequency spectrum. In cases where the value of l is infinitely large (which is not the case in practice), the autocorrelation function of the PRBS is a triangle train, as shown in Fig. 2(b) [19]. Accordingly, the continuous power spectral density (PSD) of the PRBS, or the Fourier transform of the autocorrelation function of the PRBS, contains many spectral peaks, as shown in Fig. 2(c). Fig. 2(c) also shows that the frequency locations of the spectral peaks correspond to a fundamental frequency of $1/(l \cdot T_b)$ and its harmonics and that the magnitudes of the peaks are determined by a sinc^2 envelope function. In comparison with the continuous PSD, the discrete PSD of an incoherently subsampled PRBS suffers from signal aliasing, making the resultant spectrum even more complex. An example of such discrete PSD is shown in Fig. 2(d), where the fundamental discrete frequency is denoted by f_d. Finding the value of f_d, however, is a challenging due to the complex and rich spectrum of discrete PRBSs. The remainder of this section introduces a new method for precisely determining the value of f_d.

1) f_d Coarse Estimation (Windowed DFT and Spectral Interpolation): In f_d coarse estimation, the value of f_d is identified by locating the fundamental spectral peak in the DFT spectrum of the sampled signal [20]. The spectral peak corresponding to f_d, shown in Fig. 2(e), however, may consist of a few adjacent spectral components, not a single value, due to the spectral leakage caused by the incoherency of sampling. Reducing such spectral leakage can be achieved by applying various window functions to the sampled signal. In this section, the Gaussian window function is used since the use of the Gaussian time window ($\sigma = 1/8$) in combination with the Gaussian interpolation in the frequency-domain (to be described later) results in the lowest frequency estimation error as summarized in [20]. The Gaussian window vector, $\mathbf{w} = [w[1]\ w[2]\ w[3]\ \ldots\ w[n]]^{\mathsf{T}}$, is defined as

$$w[k] = e^{-(k-n/2)^2/(2\sigma^2)} \quad \text{for } k = 1, 2, \ldots, n \tag{5}$$

where $\sigma = 1/8$. The time-windowed discrete-time signal is obtained by

$$\mathbf{x}_w = [w[1]x[1]\ \ w[2]x[2]\ \ldots\ w[n]x[n]]^{\top}. \tag{6}$$

Let

$$\mathbf{e}(\omega) := \frac{1}{\sqrt{n}}[1\ e^{j\omega}\ e^{j2\omega}\ \ldots\ e^{j\omega(n-1)}]^{\mathsf{T}} \tag{7}$$

denote a normalized vector containing regular samples of a complex sinusoid with angular frequency $\omega \in [0, 2\pi)$. The DFT basis is defined as

$$\Psi_0 := [\mathbf{e}(0)\ \ \mathbf{e}(\Delta_f)\ \ \mathbf{e}(2\Delta_f)\ \ldots\ \mathbf{e}(2\pi - \Delta_f)] \tag{8}$$

where Δ_f denotes the spectral resolution defined by

$$\Delta_f = \frac{2\pi}{n}. \tag{9}$$

The DFT magnitude spectrum of the length-n signal $\mathbf{x_w}$ is given by

$$\mathbf{S}_0 = \text{abs}\left(\Psi_0{}^{\mathsf{T}}\mathbf{x}_w\right) \tag{10}$$

where abs$(\cdot)$ computes the element-wise magnitude of a complex vector.

In Fig. 2(e) [an enlarged view of Fig. 2(d)], m denotes the discrete frequency index of the fundamental peak in the spectrum $\mathbf{S}_0 = [S_0[1]\ S_0[2]\ S_0[3]\ \ldots\ S_0[n]]^{\mathsf{T}}$. To estimate the value of f_d, we use three-point interpolation [20]. The Gaussian three-point interpolation can be used to obtain a f_d coarse estimate as

$$\dot{f}_{d,\text{coarse}} = \Delta_f \cdot \left(m + \frac{\ln \frac{S_0[m+1]}{S_0[m-1]}}{2 \cdot \ln \frac{S_0[m]^2}{S_0[m+1]S_0[m-1]}} \right) \in [0, \pi) \tag{11}$$

where $S_0[m]$ denotes the spectral magnitude at the frequency index (m).

Even though the f_d estimation described above is intended to be performed as accurately as possible, the estimation accuracy is inevitably limited by the given spectral resolution Δ_f (or spectral leakage) and the potential presence of aliased tones adjacent to the fundamental tone; hence, the procedure is called f_d coarse estimation.

2) f_d Fine Estimation (Selective DFT Frame): In this section, we introduce a method to further enhance the frequency resolution of spectral analysis to estimate f_d with better accuracy. A well-known technique to reduce digital spectral leakage and to enhance the accuracy of frequency estimation is to employ a redundant frame called a DFT frame [21]. Since we are interested in estimating only the discrete frequency value of a fundamental tone, not the spectrum itself, the DFT frame can be selectively applied to the limited frequency range near $\dot{f}_{d,\text{coarse}}$ (the value previously determined in Section II-C1) rather than being applied to the entire frequency spectrum. This selective spectral analysis is preferred since it significantly reduces computational burden.

The spectral resolution enhanced using the DFT frame with oversampling factor c is denoted by $\Delta_f(c)$, as

$$\Delta_f(c) = \frac{2\pi}{cn} \in (0, 2\pi/n]. \tag{12}$$

The selective DFT frame with oversampling factor c is then defined as

$$\begin{aligned}\Psi(c, p) := \ & [e(\dot{\omega} - p\Delta_f(c))\ \ldots\ e(\dot{\omega} - \Delta_f(c))\ \ e(\dot{\omega}) \\ & e(\dot{\omega} + \Delta_f(c))\ \ldots\ e(\dot{\omega} + p\Delta_f(c))]\end{aligned} \tag{13}$$

where $\dot{\omega} = 2\pi\,\dot{f}_{d,\text{coarse}}$ and p is a positive integer that defines the frequency search range. Notice that the use of DFT frames with oversampling factor c enables the algorithm to obtain c times the frequency resolution of the conventional spectral analysis, which uses the Fourier basis. The enhanced-resolution magnitude spectrum of the signal $\mathbf{x}_w$ obtained with the selective DFT frame is given by

$$\mathbf{S}(c, p) = \text{abs}\left(\Psi(c, p)^{\mathsf{T}}\mathbf{x}_w\right) \tag{14}$$

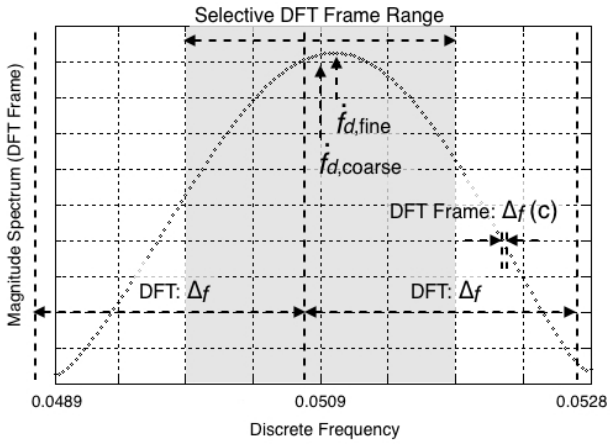

Fig. 3. DFT-frame-based magnitude spectrum (frequency span = $\Delta_f(c) \cdot 64$, oversampling ratio $c = 64$) and the obtained f_d fine estimate (a ≈3.23-Gb/s 127-bit PRBS without jitter was subsampled at 1 Gsps, and 2048 discrete samples are used).

where abs$(\cdot)$ computes the element-wise magnitude of a complex vector.

The computer simulation (a ≈3.23-Gb/s 127-bit PRBS was subsampled at 1 Gsps, and 2048 discrete samples were used) shown in Fig. 3 illustrates the enhanced spectral resolution of the selective DFT-frame-based spectral analysis. Fig. 3 shows a DFT-frame-based magnitude spectrum of signal $\mathbf{x}_w$, which spans a digital frequency range of Δ_f with a center value of $\dot{f}_{d,\text{coarse}}$ ($c = 64$ and $p = c/2$). It is found that the magnitude of the frequency component at $\dot{f}_{d,\text{coarse}}$ is not a local maximum, which indicates that $\dot{f}_{d,\text{coarse}}$ is not accurate enough with respect to the enhanced frequency resolution obtained with a DFT-frame-based spectrum. A new f_d estimate ($\dot{f}_{d,\text{fine}}$) is obtained by locating a local maximum of the plot shown in Fig. 3. In this particular example, the estimation error is $\Delta_f(c) \cdot r$, where $r = 4$ as

$$\dot{f}_{d,\text{fine}} = \dot{f}_{d,\text{coarse}} + \Delta_f(c) \cdot r \quad \in [0, \pi). \tag{15}$$

In addition, the computation process of the proposed f_d fine estimation can be further optimized using iterative methods for carrying out a local search [22]. The use of iterative methods is plausible since the envelope of the DFT-frame-based magnitude spectrum is smooth and can be modeled as a continuously differentiable function. Details of the iterative local search are not described in this paper.

3) Discrete-Time Remapping: The discrete frequency estimate $\dot{f}_{d,\text{fine}}$ obtained from Section II-C2 is used for discrete-time remapping of raw sample sequence $\mathbf{x}$ into a single period of the waveform in the discrete-time-domain. This single period corresponds to a range $[0, 2\pi)$. The remapped discrete-time value of the kth sample $x[k]$ is given by

$$\begin{aligned}t_d[k] = \text{mod}(\, & t_d[k-1] + \dot{f}_{d,\text{fine}}\ ,\ 2\pi\ ) \\ & \text{for } k = 2, 3, \ldots, n\end{aligned} \tag{16}$$

where $t_d[1] = 0$, and the modulo operation mod(x, y) returns $(x - n \cdot y)$, where n is the greatest integer less than or equal to (x/y). We use a vector to denote the remapped discrete-time values: $\mathbf{t}_d = [t_d[1]\ t_d[2]\ t_d[3]\ \ldots\ t_d[n]]^{\mathsf{T}}$. Each element of

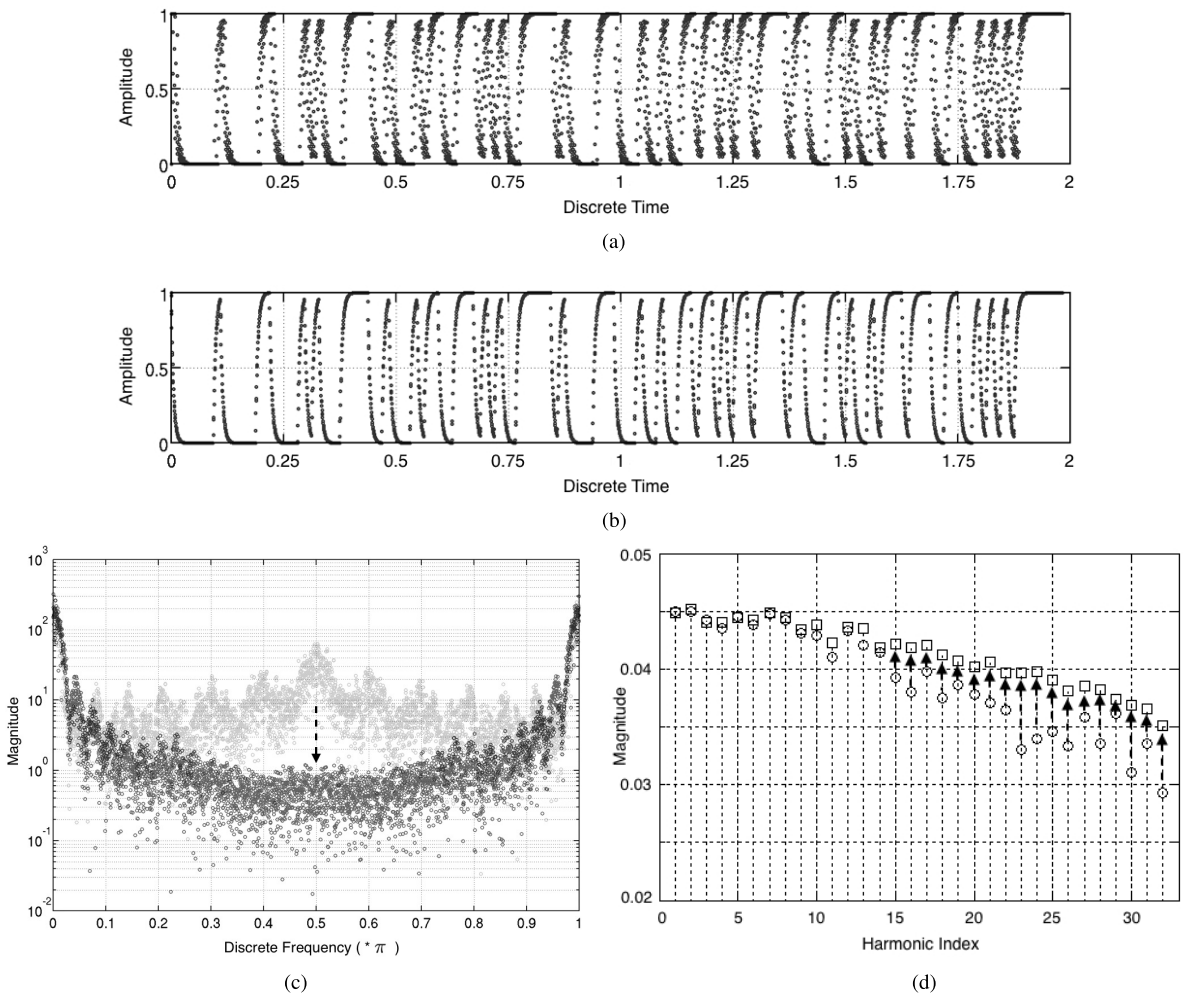

Fig. 4. Simulation results for the proposed algorithms of discrete frequency measurement: A ≈3.23-Gb/s 127-bit digital signal without jitter is sampled at 1 Gsps. The spectrum in (c) is evaluated using a nonequispaced DFT algorithm, for presentation purpose, not the proposed selective spectral analysis technique using spectral jitter cost functions. (a) Reconstructed waveform using the discrete frequency value determined by the f_d fine estimation in Section II-C2. (b) Reconstructed waveform using the discrete frequency value determined by the f_d fine tuning in Section II-C4. (c) Total nonequispaced spectrum (illustrating sparsity promotion): the spectrum of (a) denoted by the marks with light gray and the spectrum of (b) indicated by the marks with dark gray. (d) Selective nonequispaced harmonic spectrum (the fundamental discrete frequency bin and its harmonic components), which is used in this paper for enhanced computational efficiency. The spectrum of (a) denoted by the circular marks and the spectrum of (b) indicated by the square marks.

$\mathbf{t}_d$ denotes the remapped discrete-time value of each element of $\mathbf{x}$. Therefore, this pair of arrays represents a reconstructed signal in the discrete-time-domain.

Even though the discrete-frequency fine estimate, $\dot{f}_{d,\text{fine}}$, is relatively accurate, it may show a certain amount of estimation error when the fundamental discrete frequency component, which is essential to $\dot{f}_{d,\text{fine}}$ estimation, is distorted by aliased signals (due to subsampling) and noise. Because of such possible errors in $\dot{f}_{d,\text{fine}}$, the reconstructed waveform may contain reconstruction errors, which in turn result in discrete-time dispersion of the point samples in the reconstructed signal. In computer simulation, a ≈3.23-Gb/s 127-bit PRBS is subsampled at 1 Gsps and remapped to the discrete-time-domain using an f_d fine estimate. As shown in Fig. 4(a), the remapped waveform contains timing distortion, which is presented as the horizontal dispersion of the remapped samples. Since the original continuous-time PRBS does not contain any jitter in this example, it can be concluded that the timing distortion of the remapped waveform is solely induced by errors in $\dot{f}_{d,\text{fine}}$.

4) f_d Fine Tuning (Sparsity Promotion Using a Spectral Jitter Cost Function): In this section, we introduce a technique that helps further reduce the amount of reconstruction errors that may be observed in Section II-C3, especially when the signal being sampled contains a certain amount of jitter, which compromises the accuracy of the fine f_d estimation; hence, the procedure is called f_d fine tuning.

In f_d fine tuning, the best estimate of f_d is found by searching for the f_d value where the spectral leakage of the discrete spectrum of the reconstructed PRBS is minimized. This approach is enabled by the fact that a reconstructed signal that contains discrete-time jitter or dispersion due to errors in estimating $f_{d,\text{fine}}$ [as shown in Fig. 4(a)] results in additional spectral leakage in the discrete spectrum [denoted by the light gray circles in Fig. 4(c)], which in turn reduces the sparsity of the spectrum. In other words, a reconstructed

signal with the sparsest spectrum is considered the optimal reconstruction.

The spectrum evaluation of the reconstructed signal, however, requires modification of the existing spectral analysis techniques designed for equally spaced signal samples since the reconstructed signal contains nonequispaced samples to which the standard DFT techniques cannot be directly applied. For illustration purpose in this section, one of the available nonequispaced DFT algorithms [23] is used to construct the spectrum of the reconstructed signal shown in Fig. 4(c). However, the nonequispaced DFT algorithm is not computationally efficient (since it mostly requires several steps of interpolation of the reconstructed signal in addition to the standard DFT computation) and cannot be used as part of the proposed method. For this reason, we propose a selective nonequispaced spectral analysis technique. As shown in Fig. 4(d), we construct the discrete spectral components at only a few predefined locations of frequency bins, including the fundamental (discrete) frequency of the reconstructed signal and its harmonics, e.g., up to thirty second order. In this computation process, the discrete Fourier basis functions required for evaluating discrete spectral components at the selective frequency bins need to be redefined for nonequispaced sample points (since the reconstructed signal samples are nonequispaced) as

$$\begin{aligned}
\mathbf{e}_{1,\text{nonequi}} &:= \frac{1}{\sqrt{n}}\left[e^{jt_d[0]}\ e^{jt_d[1]}\ e^{jt_d[2]}\ \ldots\ e^{jt_d[n-1]}\right]^{\mathsf{T}} \\
\mathbf{e}_{2,\text{nonequi}} &:= \frac{1}{\sqrt{n}}\left[e^{j2t_d[0]}\ e^{j2t_d[1]}\ e^{j2t_d[2]}\ \ldots\ e^{j2t_d[n-1]}\right]^{\mathsf{T}} \\
&\ldots \\
\mathbf{e}_{32,\text{nonequi}} &:= \frac{1}{\sqrt{n}}\left[e^{j32t_d[0]}\ e^{j32t_d[1]}\ e^{j32t_d[2]}\ldots\ e^{j32t_d[n-1]}\right]^{\mathsf{T}}.
\end{aligned} \tag{17}$$

The use of selective nonequispaced frequency bases requires the real-time computation of the frequency bases when the algorithms are implemented in DSPs because the sample locations of the reconstructed signal, $t_d[0], t_d[1], t_d[2], \ldots$, are unique for every reconstruction. However, the number of the required frequency bases is small (the use of 32 basis functions is found to be a good choice throughout our experiments) so that this optional tuning process becomes practical. The selective nonequispaced spectral analysis is performed as

$$\Psi_{\text{nonequi}} := [\mathbf{e}_{1,\text{nonequi}}\ \mathbf{e}_{2,\text{nonequi}}\ \ldots\ \mathbf{e}_{32,\text{nonequi}}] \tag{18}$$

$$\mathbf{S}_{\text{nonequi}} = \text{abs}\left(\Psi_{\text{nonequi}}{}^{\mathsf{T}}\mathbf{x}\right) \tag{19}$$

where abs(·) computes the element-wise magnitude of a complex vector. Notice that the raw sample data ($\mathbf{x}$) is used without resequencing or time-domain filters. Resequencing the sample data are not required since the frequency basis functions are already redefined in (17) to accommodate the remapped discrete-time values $t_d[k]$. In addition, a time-window is not required because the remapped discrete-time sequence $t_d[k]$ already represents a single cycle of the sampled signal so that the remapped sample set is coherent and consequently does not produce any digital spectral leakage.

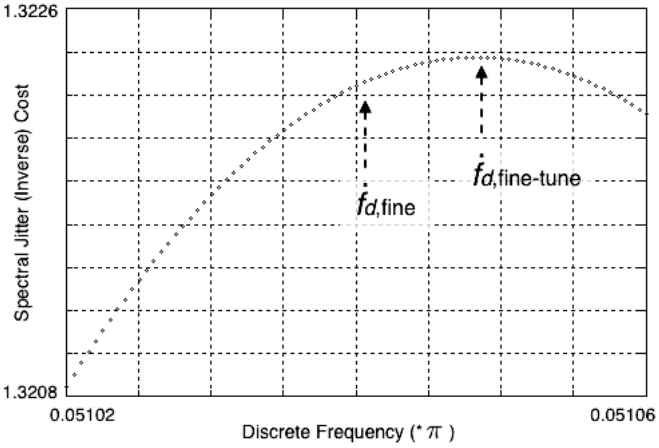

Fig. 5. Spectral jitter cost function, in the f_d fine tuning (Section II-C4), obtained using the proposed selective nonequispaced harmonic spectral evaluation. The discrete spectral resolution of the jitter cost function in this particular example is $\approx 5e\text{-}8\cdot\pi$ when the DFT frame resolution $\Delta_f(c = 64)$ is $\approx 3e\text{-}5\cdot\pi$ (a ≈3.23-Gb/s 127-bit PRBS without jitter was subsampled at 1 Gsps, and 2048 discrete samples are used).

The main reason for using the proposed spectral jitter cost function comes from the fact that when the spectrum of the reconstructed signal is observed only in the selective frequency bins, i.e., the fundamental frequency bin and its harmonics ($\mathbf{S}_{\text{nonequi}}$), the sparsest total spectrum corresponds to the greatest sum of the spectrum magnitude values at those selective frequency bins. This is because the optimal reconstruction corresponds to the reconstructed signal with minimal discrete-time jitter or dispersion, as shown in Fig. 4(b), as compared with the nonoptimal reconstruction in Fig. 4(a), and because the optimal reconstruction in turn results in the least spectral leakage (or the sparsest spectrum) in the frequency-domain, as shown in Fig. 4(c). In f_d fine tuning, the sum of these spectrum magnitude values is used as a cost function, called the spectral jitter cost function. The fine tuning algorithm using the spectral jitter cost function works well, even in the presence of the timing noise of the test signal, since the algorithm is intended to find the optimal reconstruction by reducing the jitter quantity of the reconstructed signal whether the jitter originates from the signal itself or is the digital jitter caused by reconstruction errors.

The best reconstructed PRBS can be found by sweeping the discrete frequency value in the range of $[\dot{f}_{d,\text{fine}} - \Delta_{f_{\text{tune}}}/2, \dot{f}_{d,\text{fine}} + \Delta_{f_{\text{tune}}}/2]$, where $\Delta_{f_{\text{tune}}}$ denotes the range of the discrete frequency sweep. Notice that the range of discrete frequency sweep used in this section can be relatively small because $\dot{f}_{d,\text{fine}}$ is already accurate, because of its enhanced frequency resolution obtained with the oversampling factor (c). Among many different versions of the remapped discrete-time sequence obtained by sweeping the discrete frequency estimation value, the one with the greatest sum of the discrete spectrum magnitude $\mathbf{S}_{\text{nonequi}}$ results in the optimally reconstructed PRBS. As shown in Fig. 5, the f_d fine tuning using a spectral jitter cost function results in $\dot{f}_{d,\text{fine-tune}}$, which is an f_d estimate with even enhanced accuracy, when compared with $\dot{f}_{d,\text{fine}}$.

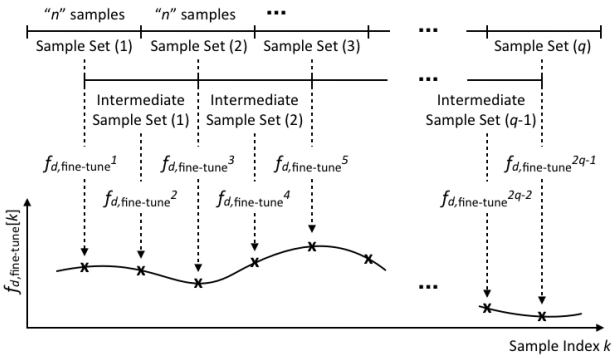

Fig. 6. Frequency estimation is conducted on q consecutive sample sets (N consecutive samples are shown in total, where $N = nq$ and q is a positive integer) and on $q - 1$ intermediate sample sets (denoted below the regular sample sets). Each sample set contains n samples.

5) Long-Term Jitter Compensation: An equivalent-time digital oscilloscope generally uses a clock signal that is phase/frequency-synchronized with the analog signal being tested as a sampling time-base. This sampling time-base signal contains almost the same long-term jitter content as that of the test signal. For this reason, when the test signal is sampled using the synchronized sampling time-base, the long-term jitter of the test signal can be automatically cancelled out and barely measured by the oscilloscope. By contrast, the proposed jitter characterization technique does not incorporate any synchronization hardware (note that, we employ incoherent subsampling), and the quality of signal reconstruction may be compromised by its long-term jitter when a large number of consecutive samples is used for signal reconstruction. To solve the issue, in this section, we use a digital postprocessing technique to compensate the reconstructed signal for the long-term jitter contained in both the test signal and the sampling time-base.

Before describing the details of the proposed method, we briefly introduce the principle of long-term jitter. Jitter is a value that accumulates over time, so its jitter time series behaves as a random walk as shown in Fig. 7(a), which is obtained using computer simulation. As shown in the figure, the jitter time series is not bounded and contains long-term as well as short-term jitter components. In cases where long-term jitter components are predominant in overall jitter, a reconstructed waveform may contain discrete-time dispersion to the extent that the waveform is hardly recognizable. We address this issue by compensating the reconstructed waveform for its long-term jitter components. Details of the long-term jitter compensation are described in the following paragraph.

For long-term jitter compensation, we use N number of consecutive samples (where $N = nq$ and q is a positive integer) as shown in Fig. 6 and measure the time-varying discrete frequency of the signal ($\dot{f}^1_{d,\text{fine-tune}}, \dot{f}^2_{d,\text{fine-tune}}, \ldots$) where each frequency estimate is obtained by employing the same technique used in Section II-C4. We also use a sliding window that can be found in the short-time Fourier transform, where the Fourier transform of local selections of the sampled signal is performed using a sliding time window. In this section, we use a time window that slides by $n/2$ sample points every frequency estimation, as shown in Fig. 6. The discrete frequency of each local selection is estimated using the algorithms used in Section II-C. The estimated discrete frequency value may vary over time windows due to the long-term jitter of the sampled signal. The obtained discrete frequency estimates over time windows form a time-varying discrete frequency, which can be used for the long-term jitter compensation.

In computer simulation, a random jitter time series is generated as shown in Fig. 7(a) and injected into the time-base that was used for generating a ≈3.23 Gb/s, 127-bit PRBS. The PRBS is then incoherently subsampled at 1 Gsps without sampling jitter. The time-varying frequency estimates $\dot{f}^1_{d,\text{fine-tune}}, \dot{f}^2_{d,\text{fine-tune}}, \ldots$ are obtained, and these coarse estimates are interpolated to N sample points, which results in $\dot{f}_{d,\text{fine-tune}}[k]$, where k denotes the sample index. The obtained $\dot{f}_{d,\text{fine-tune}}[k]$ is then translated to the remapped discrete-time value $t_d[k]$ using

$$t_d[k] = \text{mod}(\, t_d[k-1] + \dot{f}_{d,\text{fine-tune}}[k]\,,\; 2\pi\,) \quad \text{for } k = 2, 3, \ldots, N \tag{20}$$

where $t_d[1] = 0$ [notice that (20) is a modification of (16)]. Fig. 7(a) shows the variation in $t_d[k]$ after the variation is rescaled to the continuous time-domain for comparison purpose. The figure shows that plot (b) tracks the long-term components of plot (a). Because of this long-term jitter tracking effect, the reconstructed signal obtained from (20) is the waveform that is automatically compensated for its long-term jitter.

The long-term jitter compensation can also be observed in the spectrum domain. In Fig. 7(b), plots (a) and (b) show the PSDs of a (carrier) signal that contains the random jitter time series shown in plots (a) and (b) of Fig. 7(a), respectively. Fig. 7(b) represents the amount of jitter that is compensated with the proposed jitter tracking method. Therefore, the difference between the two PSD functions shown in Fig. 7(b) represents the amount of jitter contained in the reconstructed signal after long-term jitter compensation.

D. Self-Reference Signal Extraction

A (timing) reference signal is required to enable jitter quantification of the reconstructed waveform. In this paper, however, we assume that an external timing reference signal cannot be provided. To overcome such a limitation, we use a digital signal denoising technique to extract a self-reference signal from the reconstructed signal itself. The use of a digitally obtained self-reference signal alleviates the need for additional signal sources and timing circuitry.

We use a wavelet shrinkage (or denoising) technique to denoise a reconstructed waveform and to find its self-reference signal. Discrete wavelet transform is widely used for denoising a randomly distorted signal. Especially for phase noise reduction, noise suppression performance of wavelet shrinkage methods has been evaluated in many relevant areas of signal processing [24]. In this paper, we apply wavelet shrinkage to a reconstructed PRBS to reduce the jitter noise of the

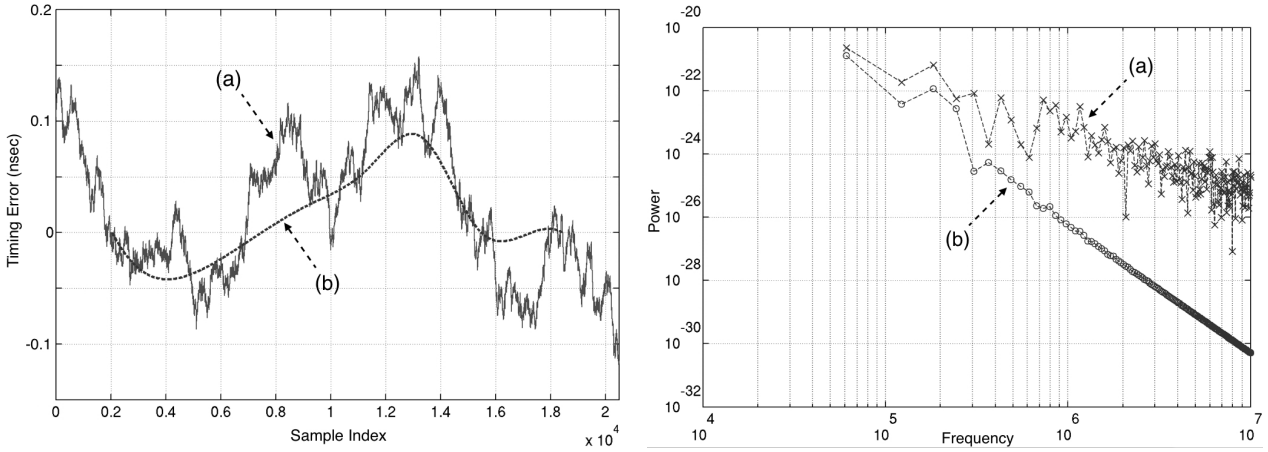

Fig. 7. Simulation results of the software CR-based jitter tracking. (a) plots (a) and (b), respectively, show a jitter time series (injected to a PRBS time-base) and software CR-based jitter tracking. (b) plots (a) and (b), respectively, show the PSD (one-sided) estimations of carrier signals with the jitter time series (a) and (b) in (a).

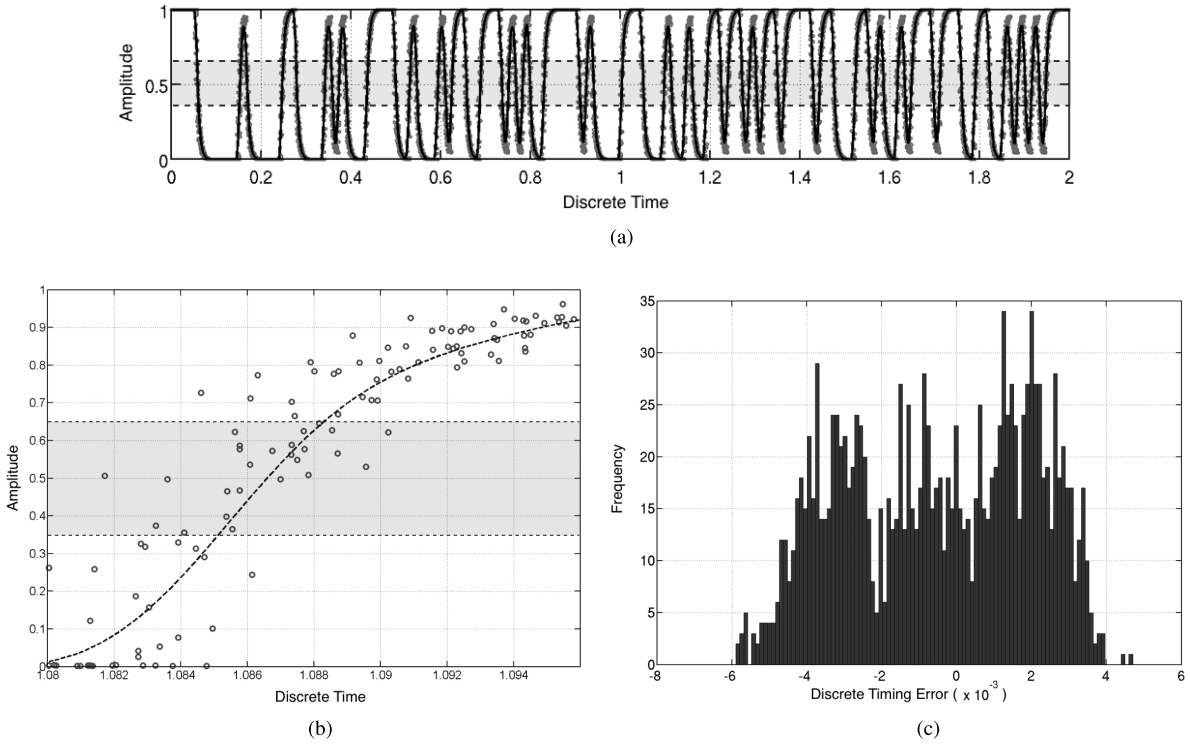

Fig. 8. Simulation results of a ≈3.23-Gb/s 127-bit digital signal with injected jitter, sampled at 1 Gsps. (a) Reconstructed waveform of a 127-bit digital pattern with jitter (circular marks) and self-reference signal (solid line). (b) Software CR-based jitter tracking (dashed line) compared with injected jitter values (solid line). (c) Jitter Histogram of the reconstructed signal shown in (a).

reconstructed signal. The obtained self-reference signal is denoted by $\mathbf{x}_r$.

In computer simulation, a ≈3.23-Gb/s, 127-bit PRBS with ≈27.69-ps rms random jitter is incoherently subsampled with 1-Gsps sampling rate, and 2^{16} discrete samples are acquired. The sampled signal is reconstructed in the discrete-time-domain with long-term jitter compensation described in Section II-C5. In Fig. 8(a), the circular marks indicate point samples of the reconstructed waveform. As shown in the figure, the reconstructed waveform contains discrete-time jitter (or dispersions) in the discrete-time-domain because of jitter of the original PRBS being sampled. Jitter noise contents of the reconstructed PRBS are removed using wavelet decomposition, and the self-reference signal can be obtained. This is possible because wavelet coefficients at low-frequency scales are dominated by signal concentration (which are used to determine the self-reference signal), whereas those at high-frequency scales mainly represent signal noise components. The bandwidth of jitter noise reduction depends on the selected wavelet decomposition level: deeper decomposition level,

TABLE I
SELF-REFERENCE SIGNALS' ABSOLUTE TIMING ERRORS MEASURED IN UIS

Wavelet (Level)	Mean ($\cdot 10^{-3}$)	Max ($\cdot 10^{-3}$)	RMS ($\cdot 10^{-3}$)
Harr (4)	0.28663	0.85078	0.19514
Harr (5)	0.26291	0.85115	0.17414
Daubechies 2 (4)	0.29504	0.87481	0.20547
Daubechies 2 (5)	0.25064	0.72870	0.15659
Daubechies 4 (4)	0.30240	0.90206	0.21260
Daubechies 4 (5)	0.24980	0.68874	0.15307
Biorthogonal 1.3 (4)	0.29504	0.87481	0.20547
Biorthogonal 1.3 (5)	0.25064	0.72870	0.15659
Discrete Meyer (4)	0.31023	0.92060	0.21967
Discrete Meyer (5)	0.25447	0.63758	0.14762

wider noise reduction bandwidth. The self-reference signal obtained in this experiment with Daubechies four-tap wavelet and five-level decomposition is denoted with a solid line in Fig. 8(a). Fig. 8(b) shows a close-up view of Fig. 8(a). Notice that the optimal selection of decomposition levels and wavelet types can be determined based on experimental results, which is not explicitly provided in this paper.

To evaluate the performance of the self-reference signal extraction (in computer simulation), we compared the obtained self-reference signal with the ideal reference signal (available as a benefit of computer simulation) to measure timing differences between the two signals in the discrete-time-domain. Table I shows the timing comparison results for various wavelets and decomposition levels. Only 30% of the signal dynamic range is used for the timing comparison, as shown in Fig. 8(a).

E. Jitter Quantification

The reconstructed signal obtained from Section II-C contains discrete-time dispersion induced by the short-term jitter of both the original continuous-time signal being sampled and the measurement system (or digitizer). Notice that the reconstructed signal has already been compensated for its long-term jitter in Section II-C5. The remaining short-term jitter of the test signal is measured by quantifying the discrete-time dispersion of the reconstructed point samples (or by comparing the time point of the reconstructed signal with that of the self-reference signal). The result is used for the total (short- and long-term) jitter time series extraction, as shown in Section II-E1. In addition, a data-dependent jitter separation method is given in Section II-E2.

1) Random Jitter Time Series Extraction: The sample dislocation of the reconstructed signal from the self-reference signal (given by Section II-D) is digitally quantified in the discrete-time-domain, which results in the reconstruction of the random jitter dynamics of the test signal. The data-dependent jitter of the test signal is separately considered in Section II-E2 but not counted here since data-dependent jitter is equally present in both the reconstructed signal and the self-reference signal. In Fig. 8(b), a rising edge of the reconstructed PRBS and its self-reference signal are shown [this is a closer view of Fig. 8(a), which is a computer simulation result]. As shown in Fig. 8(b), the point samples within a predefined amplitude range (30% of the dynamic range) are used for the discrete-time jitter quantification. This is required because the point samples adjacent to the amplitude levels of logic high and logic low are affected more by amplitude noise than by timing noise. In this manner, the amount of discrete-time sample dislocation (or jitter), denoted by ϵ_t, is calculated for all the transition edges of the reconstructed signal

$$\epsilon_t[k] = t_d[k] - t_r[k], \quad k = 1, 2, 3, \ldots \tag{21}$$

The obtained jitter time series ϵ_t is shown in a histogram in Fig. 8(c). The histogram indicates that the reconstructed PRBS contains $\approx$0.002517 (rms) discrete-time random jitter, which corresponds to $\approx$49.46 ps (rms) random jitter in the continuous-time-domain, when the injected short-term jitter components measure $\approx$51.25 ps (rms) in simulation.

The jitter time series ϵ_t can be seen directly in the discrete-time-domain to show its random dynamics as opposed to statistical characteristics.

2) Data-Dependent Jitter Calculation: The data-dependent jitter of the reconstructed signal is measured by observing the zero-crossing discrete-time of each transition edge of the self-reference signal, not the reconstructed signal samples. Since the self-reference signal is an averaged waveform (in time) of the reconstructed signal, the self-reference signal contains the same characteristic of data-dependent jitter as that of the reconstructed signal. In this approach, the jitter value of each transition edge of the reconstructed signal is individually measured so that the data-dependent jitter is automatically decomposed from the total jitter. In comparison, conventional jitter analyzers collect jitter data from all the transition edges of the sampled signal and decompose its jitter components using histogram-based jitter decomposition methods.

III. MORE CONSIDERATIONS

A. Comparison With Existing Software-Synchronization Techniques

In this section, the synchronization accuracy of the proposed algorithmic CR technique is compared with the two other techniques showing comparable performance in computer simulation. In this experiment, the optimal frequency estimate is defined as the one that results in the least amount of jitter in the reconstructed signal since the signal being sampled is supposed to contain inherent jitter. The simulation setup is similar to that shown in Fig. 5, where a $\approx$3.23-Gb/s 127-bit PRBS is subsampled at 1 Gsps, and 2048 discrete samples are used. The only difference is that random jitter (10-ps rms) is applied to the signal being sampled to effectively compare the synchronization performance of the three algorithms with each other in a noisy sampling environment. Fig. 9(a) shows the CZT-based synchronization technique [9], [10] using 512 times the frequency resolution of the standard DFT algorithm. The resultant spectrum shows a fundamental frequency estimate that is apart from the estimate generated by the proposed algorithm, which uses the spectral jitter cost function.

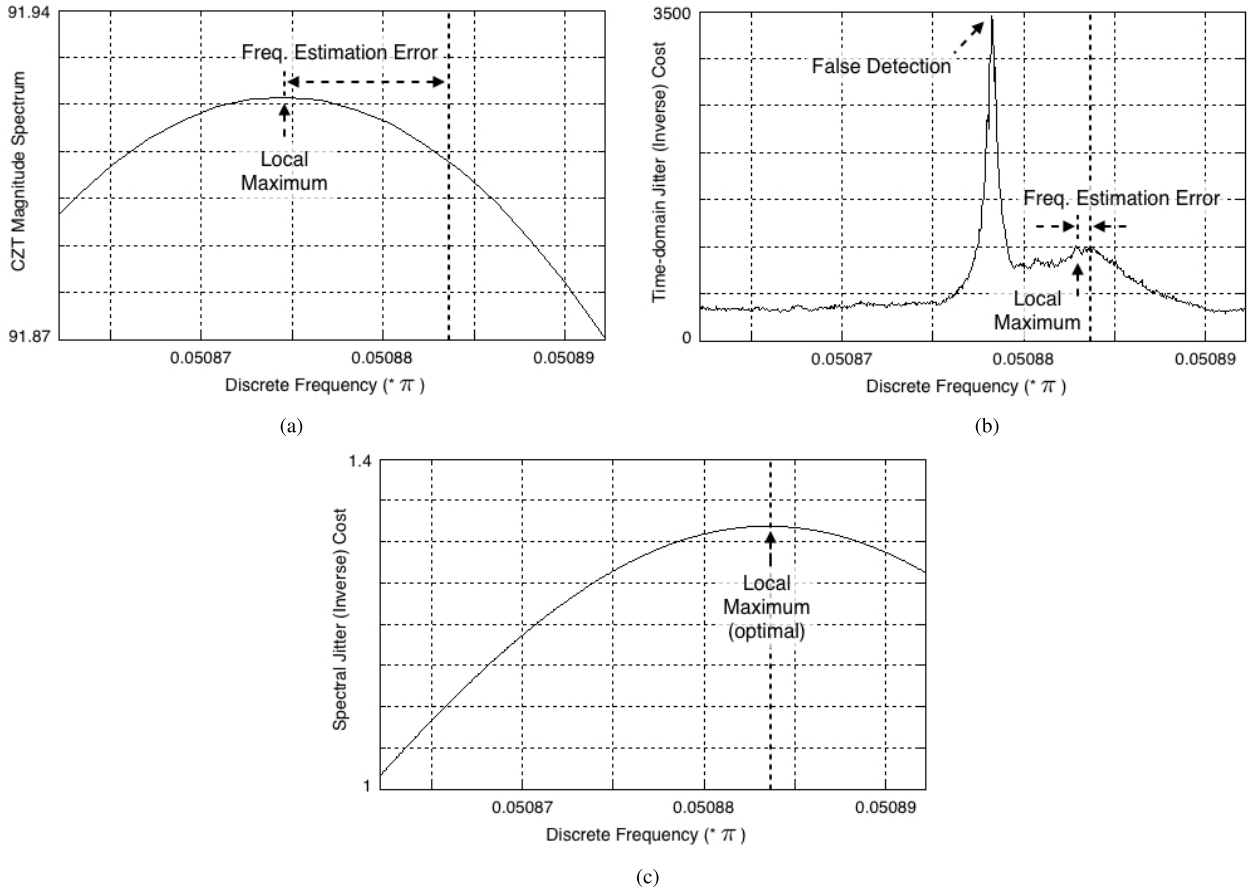

Fig. 9. Comparison between the (time-domain jitter) cost function used in [11] and the proposed spectral jitter cost function described in Section II-C4. (a) CZT-based enhanced spectral evaluation shown in [9] and [10]. (b) Time-domain jitter cost function used in [11]. (c) Proposed spectral jitter cost function.

The estimation error is $\approx$13.5E-6($\cdot\pi$). The estimation error in the CZT-based approach further increases when the fundamental tone in the spectrum is distorted by the aliased harmonic tones or other spectral distortions. Even though the estimation error is not significant in this test case, the reconstructed signal may contain noticeable timing distortions due to the accumulated errors. In comparison, the spectral jitter cost function used in the proposed CR algorithm is shown not to be affected by the aliased tones since the algorithm is based on the reconstructed discrete spectrum as opposed to the spectrum of the raw sample data. The time-domain reconstruction proves that the frequency estimate obtained from the proposed algorithm is the optimal value (associated figures not provided).

Fig. 9(b) shows the time-domain jitter cost function [11] for the same simulation setup as above. The time-domain jitter cost function may result in false frequency detection when the frequency sweep range cannot be reduced enough, which is the case when the accuracy of the initial frequency estimation (using the CZT spectrum for instance) is compromised by inherent jitter and aliased distortion spectral components. In addition, the time-domain jitter cost function is not smooth, especially when the number of samples being used is limited. If the local maximum of the time-domain cost function is successfully located, the frequency estimation error is relatively low ($\approx$1E-6($\cdot\pi$)). However, searching the local maximum in this technique is not reliable due to its nonsmooth cost function. In comparison, the spectral jitter cost function locates the optimal frequency estimate more reliably, because of its smoothness, as shown in Fig. 9(c).

B. Line Spectra Overlapping

In some cases, the line spectra of the PSD are overlapped on top of each other. Thus, the PSD is less informative in terms of the discrete frequency estimation, which compromises the accuracy of the discrete frequency estimation. The PSD of a continuous-time PRBS is shown in Fig. 11(a), and the discrete PSD obtained by incoherently subsampling the same signal is shown in Fig. 11(b). In Fig. 11(a), the frequency locations (a) and (b) are apart from f_s by f_b/l, and the (c) and (d) are apart from $2f_s$ by f_b/l. In Fig. 11(b), these frequency locations are relocated (or converged) to the discrete fundamental frequency $f_d(=(f_b/l)/(f_s/2)\cdot\pi)$ due to signal aliasing. Similarly, the spectral components of the continuous-time PRBS near frequency locations of $\lambda\cdot f_s \pm f_b/l$ ($\lambda = 1, 2, 3, \ldots$) are translated near the discrete fundamental frequency f_d in the discrete frequency-domain. If the aliased terms are located too close to f_d, which is called line spectra overlapping in this paper, identifying the exact location of

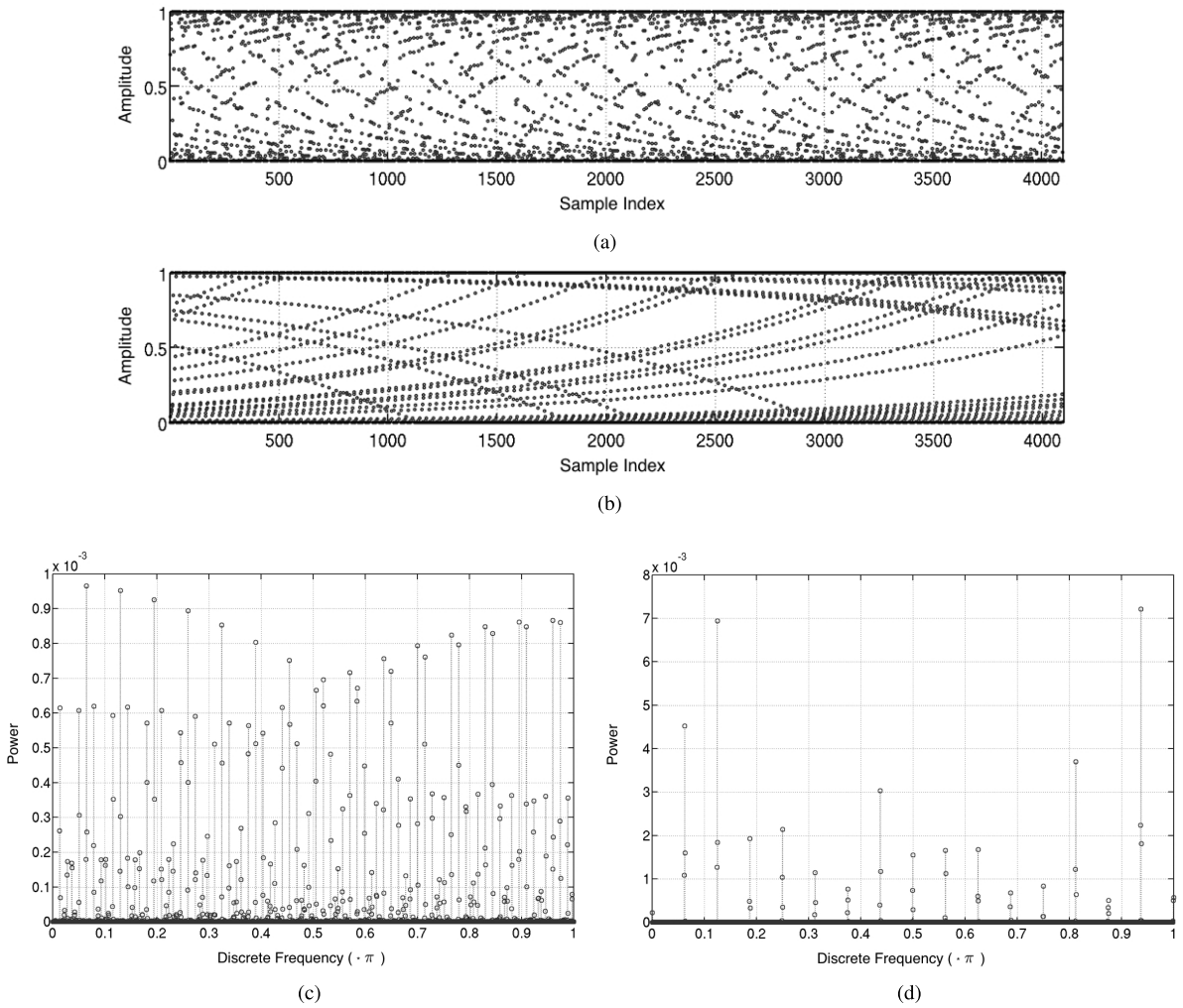

Fig. 10. Simulation results for two cases of subsampling regarding sample distribution. (a) Raw subsampled waveform of a 3-Gb/s 127-bit sequence, digitized at 727.17 Msps. (b) Raw subsampled waveform of a 3-Gb/s 127-bit sequence, digitized at 755.94 Msps (problematic sample distribution). (c) Discrete power spectrum (FFT-based, one-sided) of the subsampled waveform shown in (a). (d) Discrete power spectrum (FFT-based, one-sided) of the subsampled waveform shown in (b) (problematic spectrum).

f_d becomes problematic. The spectral components (1)–(8) in Fig. 11(a) are aliased and present near the f_d in the discrete frequency-domain in Fig. 11(b). In particular, the discrete frequency component (4) is located very close to the f_d, distorting the discrete spectrum information of the fundamental frequency (f_d).

The sampling criteria described below prevent discrete line spectra from being overlapped on the fundamental spectral component

$$\begin{aligned}\min\big(\ & |\lambda \cdot f_s - f_b/l - \beta \cdot f_b/l| \\ & |\lambda \cdot f_s - f_b/l - (\beta+1) \cdot f_b/l| \\ & |\lambda \cdot f_s + f_b/l - (\beta+2) \cdot f_b/l| \\ & |\lambda \cdot f_s + f_b/l - (\beta+3) \cdot f_b/l|\ \big) > 2f_s/n \end{aligned} \quad (22)$$

$$\beta = \left\lfloor \frac{\lambda \cdot f_s - f_b/l}{f_b/l} \right\rfloor \quad (23)$$

$$\lambda = 1, 2, \ldots, \lfloor f_b/f_s + 1 \rfloor \quad (24)$$

where f_b denotes the bit frequency ($=1/T_b$), l denotes the pattern length of the sampled PRBS, f_s denotes the sampling speed, and $\lfloor \cdot \rfloor$ denotes the floor function, which maps a real number to the next smallest integer. Equation (22) indicates that the frequency distance between the fundamental frequency replica over the multiple Nyquist zones, $\lambda \cdot f_s \pm f_b/l$, and the PRBS frequency components located close to those, $(\beta + k) \cdot f_b/l$ $(k = 0, 1, 2, 3)$, needs always to be larger than $2f_s/n$, which is twice the frequency resolution of the discrete PSD. Because of the three-point-based fundamental frequency estimation described in Section II-C1, the frequency components located at the distance of f_s/n (from the fundamental tone) result in the line spectra overlapping. This overlapping negatively contributes to the fundamental frequency estimation process. Equation (24) indicates that the sampling criteria need to be considered only for the spectrum up to f_b assuming that the power level of the spectrum beyond f_b is low enough to be negligible.

In our computer simulation, a sampled PRBS that meets the sampling criteria is generated and shown in Fig. 10(a). The PSD of the signal, shown in Fig. 10(c), does not contain frequency overlapping except the spectral components whose power levels are low enough and close to the noise floor.

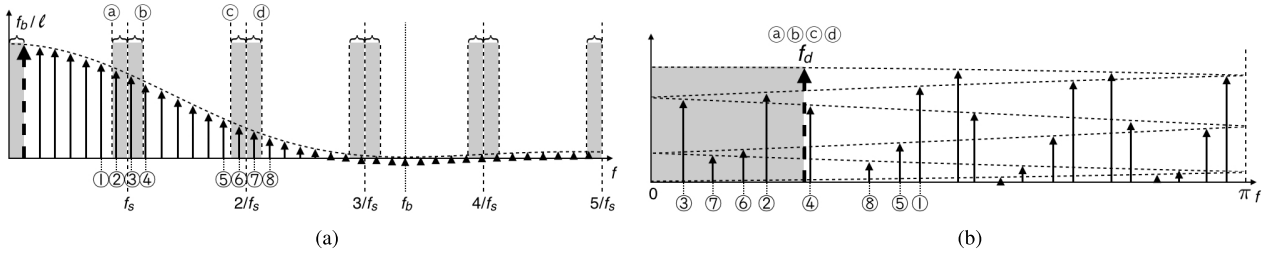

(a) (b)

Fig. 11. Line spectra overlapping with the fundamental discrete frequency component. (a) Part (up to the tenth fold of the Nyquist rate) of the PSD (one-sided) of a continuous-time PRBS. (b) Discrete PSD of the (incoherently) subsampled data of the PRBS in (a).

In such a sampling case, the fundamental frequency component can be clearly identified. In comparison, Fig. 10(b) shows a sampled PRBS whose sample points are sparsely distributed (in terms of amplitude) within a local selection of the sample index. The PSD of this sampled signal, as shown in Fig. 10(d), contains overlapped (or sparse) frequency components, which makes it less informative in terms of the discrete frequency estimation.

IV. Hardware Validation

In hardware validation, a wideband subsampling digitizer is designed using a dc 18-GHz wideband track-and-hold amplifier (Hittite HMC661LC4B) followed by a 12-bit A/D converter (Texas Instruments ADC12D1800), both set to run at 1 Gsps. In this scheme, the wideband track-and-hold amplifier is used as a front-end of the subsampling A/D converter to increase the input analog bandwidth of the digitizer system. The ≈2.853-Gb/s 31-bit PRBS test signal is generated by a digital signal generator (Agilent 81134A) whose reference time-base is phase-modulated (random and sine) using another signal generator (Agilent 4421B). The sampling clock signal of the digitizer is not synchronized in frequency with the test signal being sampled. This test setup is used for all the hardware validation processes in this section.

A. Discrete Frequency Estimation Accuracy

To characterize the performance of the proposed frequency estimation method (or corresponding jitter tracking), we applied periodic jitter components (50-kHz sinusoidal phase modulation) to the PRBS test signal and measured the accuracy of frequency estimates digitally obtained from sampled signals. The number of samples used in each analysis time window is 2048. Fig. 12 shows short-time frequency estimation for PRBS test signals with sinusoidal jitter components (details are provided in the figure caption). Since jitter frequency is only 50 kHz and can be fully tracked by the proposed jitter tracking method, any deviations in the measured frequency values compared with the reference curves (denoted by dotted lines in Fig. 12) are considered measurement error terms. The discrete frequency estimation error in this test setup is 3.77e-7 rms [notice that discrete frequency values are in the range [0,1)], which represents greatly enhanced accuracy, because of the f_d fine tuning process described in Section II-C4.

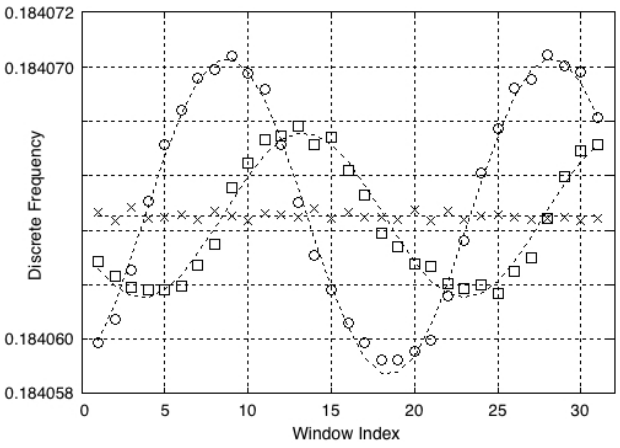

Fig. 12. Short-time frequency estimation for PRBS test signals with sinusoidal jitter components: 1) no jitter (denoted by x marks); 2) 0.4-UI(pk-pk) 50-kHz sinusoidal jitter (denoted by square marks); and 3) 0.8-UI(pk-pk) 50-kHz sinusoidal jitter (denoted by circular marks). The dotted lines represent reference curves provided for error calculation.

B. Jitter Tracking Bandwidth

As shown in Fig. 12, a periodic jitter component of 50-kHz jitter frequency is fully tracked (with a small amount of calculation error) by the proposed jitter tracking with the analysis time window of 2048 samples. In this section, we increase the number of samples to 8192 to reduce the jitter tracking bandwidth and to observe the difference between the two window sizes in terms of the remaining amount of jitter in the reconstructed eye-diagram.

Fig. 13(a) shows the jitter tracking performance comparison for the 2048-sample window (or wide jitter tracking bandwidth) and the 8192-sample window (or reduced jitter tracking bandwidth). As compared with the wide bandwidth jitter tracking results (denoted by the squares), the reduced bandwidth jitter tracking data points (denoted by the circles) show a fewer frequency estimates within the given data set and the jitter tracking curve with reduced amplitude due to the reduced jitter tracking bandwidth. Fig. 13(d) shows a reconstructed eye-diagram obtained with wide bandwidth jitter tracking while Fig. 13(c) shows an eye-diagram with an increased amount of reconstructed jitter due to the reduced jitter tracking bandwidth.

C. Jitter Decomposition

In this section, we use the reduced bandwidth jitter tracking method to show the effect of jitter decomposition.

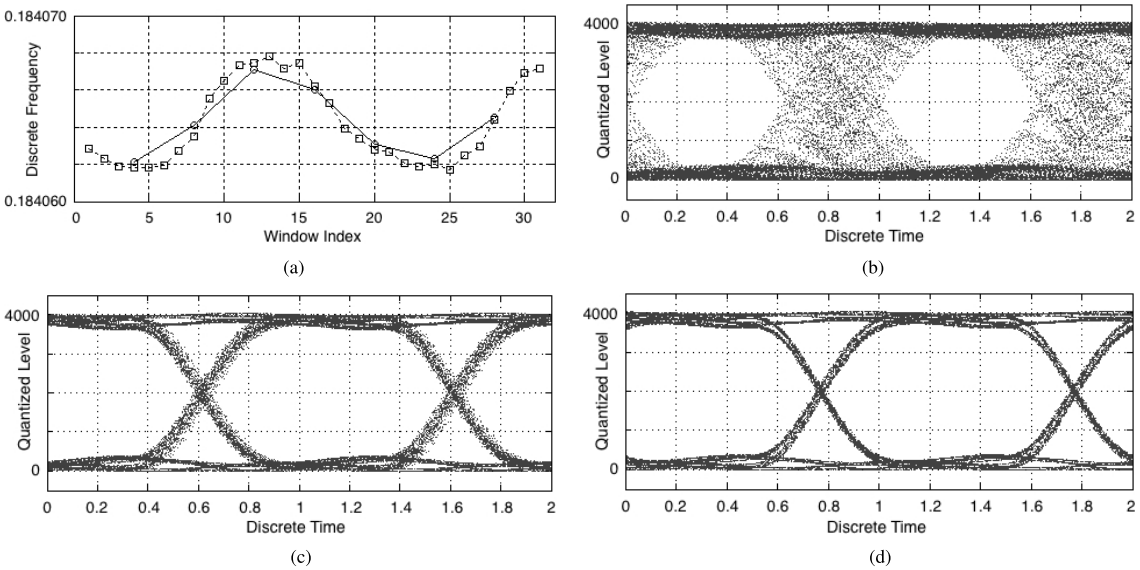

Fig. 13. Comparison between wide and reduced jitter tracking bandwidth for 0.4-UI(pk-pk) 50-kHz periodic jitter. (a) Discrete frequency estimation plots with wide tracking bandwidth (2048-sample windows used, denoted by the squares) and reduced tracking bandwidth (8192-sample windows used, denoted by the circles). (b) Eye-diagram obtained from one-time f_d estimation (=0.184064) without using jitter tracking. (c) Eye-diagram obtained from jitter tracking with reduced tracking bandwidth. (d) Eye-diagram obtained from jitter tracking with wide tracking bandwidth.

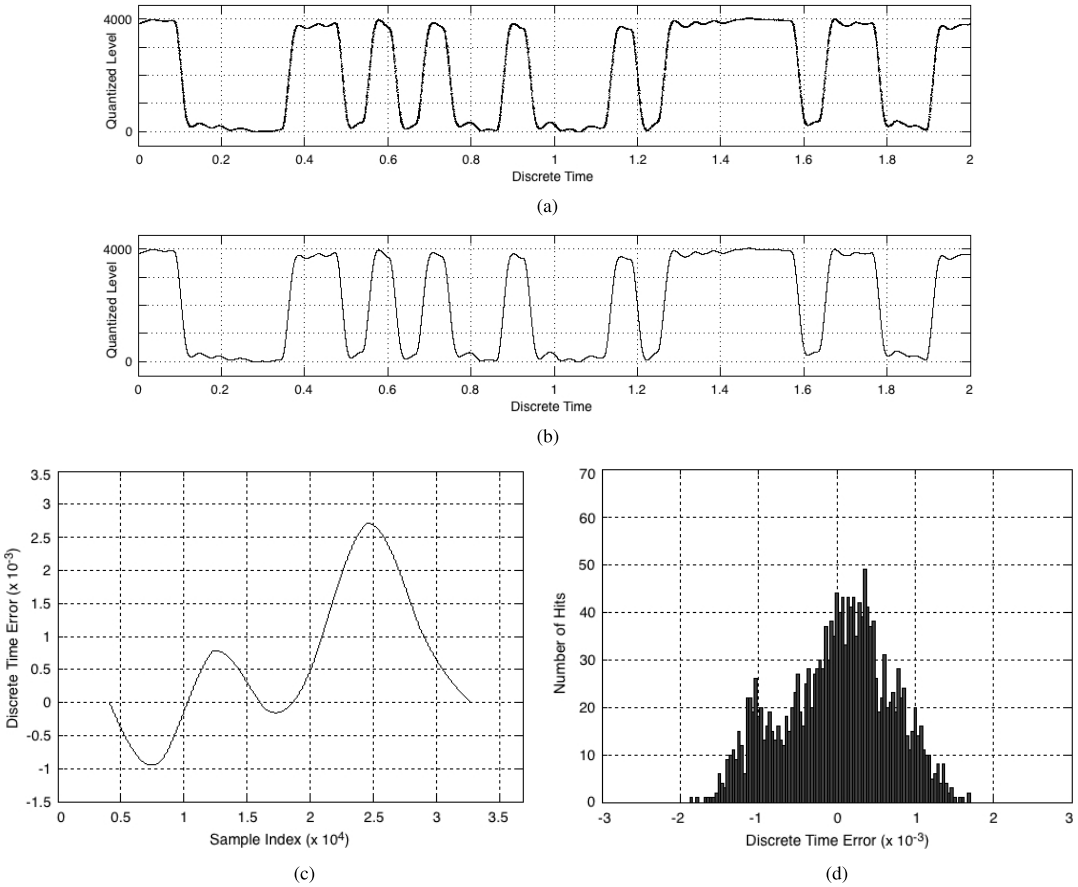

Fig. 14. Hardware validation of signal reconstruction and self-reference signal extraction for a ≈2.853-Gb/s 31-bit sequence with 0.00165 rms discrete-time random jitter. (a) Reconstructed waveform obtained using the reduced bandwidth jitter tracking (8192-sample time window). (b) Self-reference signal obtained by applying Discrete Meyer (5) wavelet denoising to the reconstructed waveform in (a). (c) Reduced bandwidth jitter tracking data sequence. (d) Jitter histogram extracted from the reconstructed waveform in (a) (after compensating for deterministic jitter components).

Fig. 14 shows a reconstructed waveform obtained using the reduced bandwidth jitter tracking and its self-reference signal derived using wavelet denoising. The deterministic jitter information can be extracted from the self-reference signal (without using conventional tail-fitting algorithms applied to jitter histograms) as summarized in Table II. Notice that the

TABLE II
DATA-DEPENDENT JITTER ESTIMATES OBTAINED FROM THE SELF-REFERENCE SIGNAL SHOWN IN FIG. 14(b) ($\cdot 10^{-3}$)

Type	E1	E2	E3	E4	E5	E6	E7	E8	E9	E10	E11	E12	E13
Discrete Meyer (5)	0.06	0.52	-0.13	-0.56	-0.76	-0.26	-0.39	0.86	-0.41	0.65	-0.88	-0.88	0.27

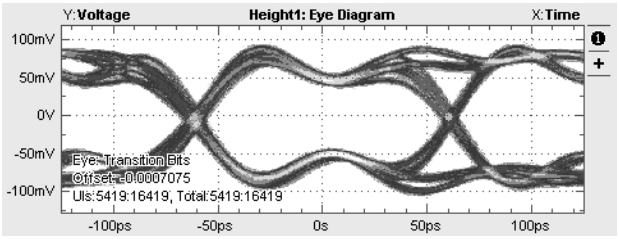

(a)

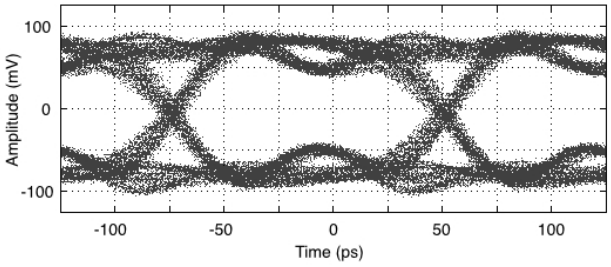

(b)

Fig. 15. Comparison between the oversampling-based CR provided by a commercial real-time oscilloscope and the proposed undersampling-based CR algorithm: a test signal of ≈8.21 Gb/s, 31-bit random pattern without jitter injection is used. (a) Eye-diagram reconstructed from oversampled (50 Gsps) data with serial data analysis toolkit of Tektronix DPO71254C (only transition bits are shown). (b) Eye-diagram reconstructed from subsampled data (2.5 Gsps) with the proposed CR algorithm without long-term jitter compensation.

accuracy of data-dependent jitter characterization is not explicitly evaluated in this section, but was previously summarized in Section II-D using computer simulation.

D. Comparison With Conventional Oversampling Real-Time Oscilloscope

In this section, we provide an experimental comparison between a conventional over-sampling software CR toolkit (serial data analysis toolkit) employed in a commercial 50-Gsps real-time oscilloscope (Tektronix DPO71254C), and the proposed subsampling algorithmic CR, in terms of signal reconstruction accuracy. To remove a potential discrepancy associated with sampling hardware measurement noise level or sensitivity, we used two independent sets of signal samples obtained from the same hardware (the sampling hardware module of Tektronix DPO71254C, whose input analog bandwidth is 12.5 GHz): 1) over-sampled data ($f_{s1} = 50$ Gsps) for the software CR module (serial data analysis toolkit) employed by Tektronix DPO71254C and 2) subsampled data ($f_{s2} = 2.5$ Gsps) for the proposed algorithmic CR. A test signal (≈8.21-Gb/s 31-bit PRBS) is generated using a LeCroy signal generator (PeRT3 Phoenix System) equipped with jitter injection capability.

A ≈8.21-Gb/s 31-bit PRBS without injected jitter is sampled independently twice with the sampling module of Tektronix DPO71254C at a sampling rate of 1) $f_{s1} = 50$ Gsps (over-sampling) and 2) $f_{s2} = 2.5$ Gsps (subsampling). The two acquired sample sets (2^{16} samples each) are postprocessed by using serial data analysis toolkit, which reconstructs an eye-diagram shown in Fig. 15(a) (only transition bits are shown), and using the proposed CR algorithm (with long-term jitter compensation), which results in another reconstructed eye-diagram shown in Fig. 15(b). Although no controlled jitter is injected to the test signal, the reconstructed eye diagrams show a certain amount of timing noise inherent to the test signal or sampling time-base. The eye-diagram in Fig. 15(a) measures 2.013-ps rms jitter on transition edges, while the eye-diagram in Fig. 15(b) measures 2.008-ps rms jitter, which shows a baseline comparison of serial data analysis toolkit and the proposed CR algorithm.

To evaluate the jitter measurement linearity both of serial data analysis toolkit ($f_{s1} = 50$ Gsps) and the proposed algorithmic CR ($f_{s2} = 2.5$ Gsps), we compared the reconstructed jitter measurements with the injected jitter values originally programmed to the test signal (≈8.21-Gb/s 31-bit PRBS) under various random jitter conditions (jitter bandwidth: 1.5–100 MHz). Fig. 16(a) shows the reconstructed (or measured) jitter values obtained from serial data analysis toolkit ($f_{s1} = 50$ Gsps), where raw measurement data are shown along with ones after compensation for inherent measurement noise to evaluate linear regression fit: The inherent measurement noise compensation is conducted in such a way that a square of the rms jitter noise measured from the test signal without jitter injection, denoted by a dotted circle in the plot, is subtracted from a square of the other measured rms jitter values with various amounts of injected jitter, assuming that the inherent measurement noise and the injected jitter are orthogonal to each other. The same test is conducted using the proposed algorithmic CR with subsampled data ($f_{s2} = 2.5$ Gsps), and its results are shown in Fig. 16(b). In addition to the jitter measurement linearity clearly shown after the inherent noise compensation both in Fig. 16(a) and (b), we found a correlation between the two methods: serial data analysis toolkit ($f_{s1} = 50$ Gsps) and the proposed algorithmic CR ($f_{s2} = 2.5$ Gsps), with a maximum error of 0.259-ps rms within the test cases conducted in this experiment.

For comparison under periodic jitter conditions, the same test setup is used for a test signal of ≈8.21-Gb/s 31-bit PRBS with 0.5-MHz, 20-ps(pk-pk) sinusoidal jitter injection: the jittered signal is sampled twice with the sampling module of Tektronix DPO71254C at a sampling rate of: 1) $f_{s1} = 50$ Gsps

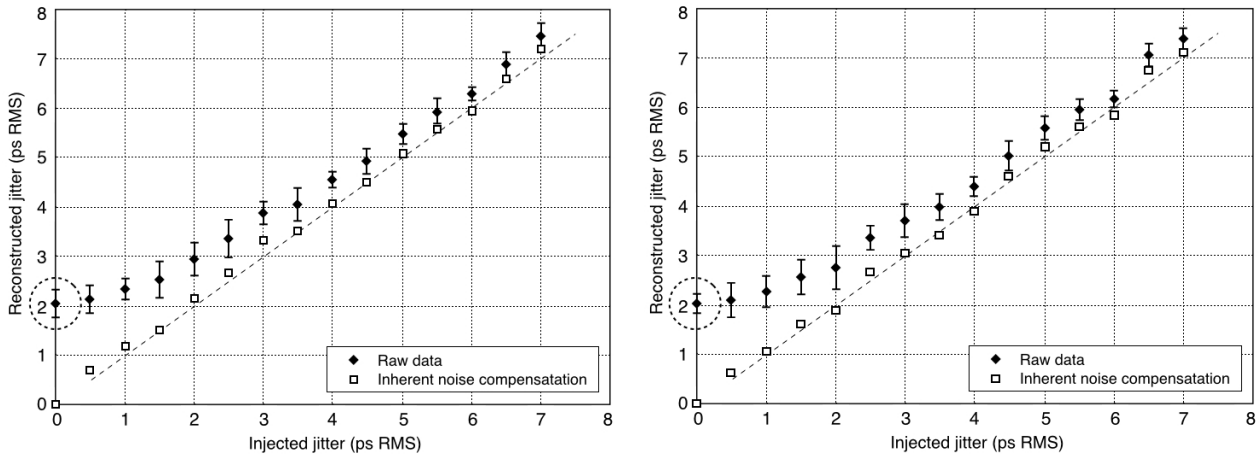

Fig. 16. Linearity evaluation of random jitter characterization of a ≈8.21-Gb/s, 31-bit random pattern: signal samples obtained from Tektronix DPO71254C with 1.5–100-MHz random jitter injection. Raw data shown with an error bar obtained from five trials conducted for each test case. (a) Serial data analysis toolkit with oversampling (50 Gsps). (b) Proposed algorithmic CR (without using long-term jitter compensation) with subsampling (2.5 Gsps).

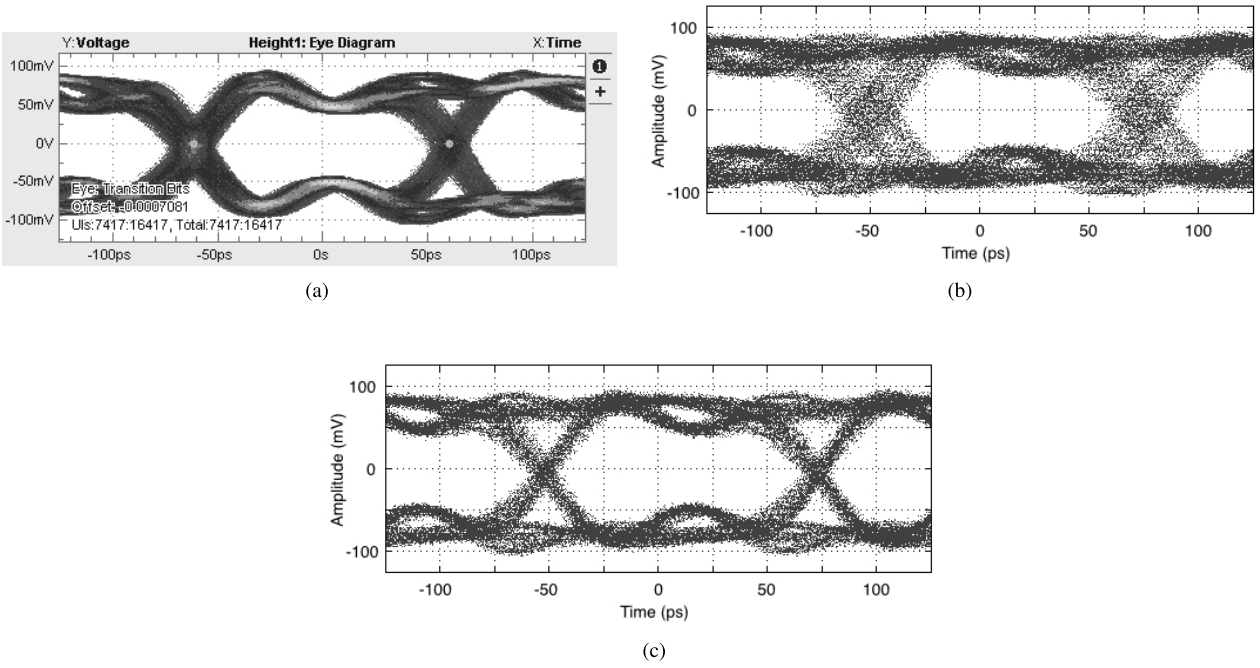

Fig. 17. Comparison between the oversampling-based CR provided by a commercial real-time oscilloscope and the proposed undersampling-based CR algorithm: a test signal of ≈8.21-Gb/s, 31-bit random pattern with 0.5 MHz, 20-ps(pk-pk) sinusoidal jitter. (a) Eye-diagram reconstructed from oversampled (50 Gsps) data with serial data analysis toolkit of Tektronix DPO71254C (only transition bits are shown). (b) Eye-diagram reconstructed from subsampled data (2.5 Gsps) with the proposed CR algorithm without long-term jitter compensation. (c) Eye-diagram reconstructed from subsampled data (2.5 Gsps) with the proposed CR algorithm with long-term jitter compensation.

(oversampling) and 2) $f_{s2} = 2.5$ Gsps (subsampling). Fig. 17(a) shows the reconstructed eye-diagram of the oversampled, jittered signal postprocessed using serial data analysis toolkit (only transition bits are shown), which shows a measured sinusoidal jitter of 20.8-ps pk-pk (when decomposed from total jitter by removing random jitter). In comparison, Fig. 17(b) and (c), respectively, show the reconstructed eye diagrams of the subsampled, jittered signal obtained using the proposed algorithmic CR without and with long-term jitter compensation (described in Section II-C5). Fig. 17(b) shows 21.2-ps pk-pk jitter (after periodic jitter decomposition), which is comparable with the measured amount of jitter in Fig. 17(a): 20.8-ps pk-pk. In addition, the eye-diagram in Fig. 17(c) is obtained using the long-term jitter compensation technique as part of the proposed CR algorithm. The eye-diagram in Fig. 17(c) does not contain injected sinusoidal jitter anymore because the long-term jitter tracking occurs on the 0.5-MHz sinusoidal jitter injected to the test signal. The residual random jitter measures 2.011-ps rms, which is comparable with the inherent jitter quantity of Fig. 15(b) (2.008-ps rms).

V. Conclusion

We proposed an enhanced algorithmic CR technique that can be applied to incoherently subsampled digital bit sequence data using the spectral sparsity analysis in the frequency-domain, which is distinct from other known methods. We evaluated the proposed technique both in simulation and hardware experiments to show the enhanced accuracy of subsampled signal reconstruction even in noisy sampling environment. In future research, we plan to extend the application of the subsampling algorithmic CR to a longer bit pattern such as PRBS-31, which is commonly used in generic high-speed digital I/O testing. The application of the algorithmic CR to a longer bit pattern may require modifications to the proposed CR algorithm, especially to the discrete-frequency estimation. In addition, a solution to the line spectra overlapping (described in Section III-B) needs to be further addressed to overcome the relevant limitation on subsampling frequency selection.

References

[1] J. R. G. Oya, F. Muñoz, A. Torralba, A. Jurado, A. Garrido, and J. Baños, "Data acquisition system based on subsampling for testing wideband multistandard receivers," *IEEE Trans. Instrum. Meas.*, vol. 60, no. 9, pp. 3234–3237, Sep. 2011.

[2] J. R. G. Oya, F. Munoz, A. Torralba, A. Jurado, F. J. Marquez, and E. Lopez-Morillo, "Data acquisition system based on subsampling using multiple clocking techniques," *IEEE Trans. Instrum. Meas.*, vol. 61, no. 8, pp. 2333–2335, Aug. 2012.

[3] M. Hartz and M. Schnecker, *Custom 2-Pole PLL*. New York, NY, USA: LeCroy Corp., Sep. 2008.

[4] K. Tan and B. A. Ward, "Signal acquisition method and apparatus using integrated phase locked loop," U.S. Patent 6 812 688, Nov. 2, 2004.

[5] L. Noirie, F. Cerou, G. Moustakides, O. Audouin, and P. Peloso, "New transparent optical monitoring of the eye and ber using asynchronous under-sampling of the signal," in *Proc. 28th ECOC*, vol. 5. Sep. 2002, pp. 1–2.

[6] G. Moustakides, F. Cerou, O. Audouin, and L. Noirie, "Eye diagram reconstruction using asynchronous imperfect sampling application to BER estimation for fiber-optic communication systems," in *Proc. 11th Euro. Signal Process. Conf.*, 2002, pp. 375–378.

[7] P. Andrekson and M. Westlund, "Nonlinear optical fiber based high resolution all-optical waveform sampling," *Laser Photon. Rev.*, vol. 1, no. 3, pp. 231–248, 2007.

[8] T. Kiatchanog, K. Igarashi, T. Tanemura, D. Wang, K. Katoh, and K. Kikuchi, "Real-time all-optical waveform sampling using a passively mode-locked fiber laser as the sampling pulse source," in *Proc. OFC Conf., Nat. Fiber Opt. Eng. Conf. OFC*, Mar. 2006.

[9] M. Aiello, A. Cataliotti, and S. Nuccio, "A chirp-z transform-based synchronizer for power system measurements," *IEEE Trans. Instrum. Meas.*, vol. 54, no. 3, pp. 1025–1032, Jun. 2005.

[10] A. Yang, J. Lai, and Y. N. Sun, "A chirp-z-transform-based software synchronization method for optical performance monitoring," *IEEE Photon. Technol. Lett.*, vol. 23, no. 22, pp. 1739–1741, Nov. 15, 2011.

[11] M. Westlund, H. Sunnerud, M. Karlsson, and P. Andrekson, "Software-synchronized all-optical sampling for fiber communication systems," *J. Lightw. Technol.*, vol. 23, no. 3, pp. 1088–1099, Mar. 2005.

[12] M. Westlund, P. Andrekson, H. Sunnerud, J. Hansryd, and J. Li, "High-performance optical-fiber-nonlinearity-based optical waveform monitoring," *J. Lightw. Technol.*, vol. 23, no. 6, pp. 2012–2022, Jun. 2005.

[13] D. Agrez, "Dynamics of frequency estimation in the frequency domain," *IEEE Trans. Instrum. Meas.*, vol. 56, no. 6, pp. 2111–2118, Dec. 2007.

[14] D. Belega, D. Dallet, and D. Petri, "Accuracy of sine wave frequency estimation by multipoint interpolated DFT approach," *IEEE Trans. Instrum. Meas.*, vol. 59, no. 11, pp. 2808–2815, Nov. 2010.

[15] L. Angrisani and M. D'Arco, "A measurement method based on a modified version of the chirplet transform for instantaneous frequency estimation," *IEEE Trans. Instrum. Meas.*, vol. 51, no. 4, pp. 704–711, Aug. 2002.

[16] H. Choi, A. Gomes, and A. Chatterjee, "Signal acquisition of high-speed periodic signals using incoherent sub-sampling and back-end signal reconstruction algorithms," *IEEE Trans. Very Large Scale Integr. (VLSI) Syst.*, vol. 19, no. 7, pp. 1125–1135, Jul. 2011.

[17] H. Choi and A. Chatterjee, "Jitter characterization of incoherently sub-sampled high-speed digital signals," in *Proc. IEEE 16th IMS3TW*, Jun. 2010, pp. 1–5.

[18] H. Choi and A. Chatterjee, "Jitter characterization of pseudo-random bit sequences using incoherent sub-sampling," in *Proc. 19th IEEE ATS*, Dec. 2010, pp. 9–14.

[19] S. Haykin, *Communication Systems*, 5th ed. New York, NY, USA: Wiley, 2009.

[20] M. Gasior and J. L. Gonzalez, "Improving FFT frequency measurement resolution by parabolic and Gaussian spectrum interpolation," in *Proc. AIP Conf.*, vol. 732. 2004, p. 276.

[21] M. Duarte and R. Baraniuk, "Spectral compressive sensing," *Appl. Comput. Harmonic Anal.*, vol. 35, no. 1, pp. 111–129, 2012.

[22] Y. Saad and Y. Saad, *Iterative Methods for Sparse Linear Systems*, vol. 620. Boston, MA, USA: PWS publishing company, 1996.

[23] J. Keiner, S. Kunis, and D. Potts, "Using NFFT 3—A software library for various nonequispaced fast Fourier transforms," *ACM Trans. Math. Softw.*, vol. 36, no. 4, p. 19, 2009.

[24] C. Martinez, X. Canovas, and M. Chandra, "SAR interferometric phase noise reduction using wavelet transform," *Electron. Lett.*, vol. 37, no. 10, pp. 649–651, May 2001.

Hyun Woo Choi (SM'06–M'10) received the B.S. degree in electrical engineering from Korea University, Seoul, Korea, in 2004, and the Ph.D. degree in electrical and computer engineering from the Georgia Institute of Technology (Georgia Tech), Atlanta, GA, USA, in 2010.

He is a Senior Engineer at Nvidia Corporation, Santa Clara, CA, USA, and an Adjunct Faculty Member with the School of Electrical and Computer Engineering, Georgia Tech. His current research interests include design-for-test, built-in self-test, diagnostics and physical characterization of advanced silicon and postsilicon devices.

Thomas Moon (SM'14) received the B.S. degree in electrical electronic engineering from the Pohang University of Science and Technology, Pohang, Korea, in 2008, and the M.S. degree in electrical and computer engineering from the Georgia Institute of Technology (Georgia Tech), Atlanta, GA, USA, in 2012, where he is currently pursuing the Ph.D. degree.

He is currently a Graduate Research Assistant with the Testing and Reliability Engineering Group, Georgia Tech. In 2014, he was an Intern with IBM, Burlington, VT, USA, where he was involved in RF test development. His current research interests include high-speed signal testing and characterization, signal integrity, and signal reconstruction by undersampling algorithm.

Abhijit Chatterjee (M'97–F'07) received the Ph.D. degree in electrical and computer engineering from the University of Illinois at Urbana-Champaign, Champaign, IL, USA, in 1990.

He served as the Chair of the VLSI Technical Interest Group at the Georgia Institute of Technology (Georgia Tech), Atlanta, GA, USA, from 2010 to 2012. He co-leads the Samsung Center of Excellence in High-Speed Design and Test established at Georgia Tech in 2011. He is a Professor with the School of Electrical and Computer Engineering, Georgia Tech. He is the Co-Founder of Ardext Technologies Inc., Tucson, AZ, USA, a mixed-signal test solutions company, where he served as the Chairman and Chief Scientist from 2000 to 2002. His work on self-healing chips was featured as one of General Electric's key technical achievements in 1992, and was cited by the *Wall Street Journal*. He has authored over 400 papers in refereed journals and meetings, and holds 20 patents. His current research interests include error-resilient signal processing and control systems, mixed-signal/RF/multi-GHz design and test, and adaptive real-time systems.

Dr. Chatterjee was a recipient of the NSF Research Initiation Award in 1993, the NSF CAREER Award in 1995, the Outstanding Faculty for Research Award from the Georgia Tech Packaging Research Center in 1996, and the Outstanding Faculty for Technology Transfer Award from the Packaging Research Center in 2000. He has received six Best Paper Awards and three Best Paper Award nominations. His group received the Margarida Jacome Award for work on VIZOR: Virtually Zero Margin Adaptive RF from the Berkeley Gigascale Research Center in 2007. He was named a Collaborating Partner in NASA's New Millennium project in 1995.